A&A, 703, A189 (2025)
https://doi.org/10.1051/0004-6361/202555842

Astronomy & Astrophysics

H_3^+ in irradiated protoplanetary disks: Linking far-ultraviolet radiation and water vapor

Javier R. Goicoechea[1,⋆], Octavio Roncero[1], Evelyne Roueff[2], John H. Black[3], Ilane Schroetter[4], and Olivier Berné[4]

[1] Instituto de Física Fundamental (CSIC). Calle Serrano 121–123, 28006, Madrid, Spain
[2] LUX, Observatoire de Paris, Université PSL, Sorbonne Université, CNRS, 92190 Meudon, France
[3] Chalmers University of Technology, Onsala Space Observatory, Onsala, Sweden
[4] Institut de Recherche en Astrophysique et Planétologie, Université de Toulouse, CNRS, CNES, Toulouse, France

Received 6 June 2025 / Accepted 20 September 2025

ABSTRACT

The likely JWST detection of vibrationally excited H_3^+ emission in Orion's irradiated disk system d203-506 raises the important question of whether cosmic-ray ionization is enhanced in disks within clustered star-forming regions, or whether alternative mechanisms contribute to H_3^+ formation and excitation. We present a detailed model of the photodissociation region (PDR) component of a protoplanetary disk – comprising the outer disk surface and the photoevaporative wind – exposed to strong external far-ultraviolet (FUV) radiation. We investigate key gas-phase reactions involving excited H_2 that lead to the formation of H_3^+ in the PDR, including detailed state-to-state dynamical calculations of reactions $H_2(v \geq 0) + HOC^+ \rightarrow H_3^+ + CO$ and $H_2(v \geq 0) + H^+ \rightarrow H_2^+ + H$. We also consider the effects of photoionization of vibrationally excited $H_2(v \geq 4)$, a process not previously included in PDR or disk models. We find that these FUV-driven reactions dominate the formation of H_3^+ in the PDR of strongly irradiated disks, largely independently of cosmic-ray ionization. The predicted H_3^+ abundance in the disk PDR peaks at $x(H_3^+) \gtrsim 10^{-8}$, coinciding with regions of enhanced HOC^+ and water vapor abundances, and is linked to the strength of the external FUV field (G_0). The predicted H_3^+ column density ($\lesssim 10^{13}$ cm^{-2}) agrees with the presence of H_3^+ in the PDR of d203-506. We also find that formation pumping, resulting from exoergic reactions between excited H_2 and HOC^+, drives the vibrational excitation of H_3^+ in these regions. We expect this photochemistry to be highly active in disks where $G_0 > 10^3$. The H_3^+ formation pathways studied here may also be relevant in the inner disk region (near the host star), in exoplanetary ionospheres, and in the early Universe.

Key words. astrochemistry – protoplanetary disks – ISM: molecules – photon-dominated region (PDR)

1. Introduction

Most protoplanetary systems form in stellar clusters (Lada & Lada 2003) and are therefore eventually exposed to external ultraviolet (UV) radiation from nearby massive stars (e.g., Winter & Haworth 2022). UV irradiation can influence the disk's chemical composition (Walsh et al. 2013; Boyden & Eisner 2020, 2023; Berné et al. 2023, 2024), impact gas line excitation (Zannese et al. 2024; Goicoechea et al. 2024), and alter the potential for planet formation. In particular, external UV radiation leads to disk mass loss driven by photoevaporative winds (Johnstone et al. 1998; Störzer & Hollenbach 1999), which truncate the outer disk, reduce the mass reservoir for planet formation, and impact the properties of gas giant planets forming within those disks (e.g., Winter et al. 2022; Qiao et al. 2023; Huang et al. 2024). However, the extent to which environmental UV radiation affects chemical processing and gas ionization remains controversial (e.g., Ramírez-Tannus et al. 2023; Díaz-Berríos et al. 2024; Schroetter et al. 2025a). This is a relevant question in the context of Solar System formation, as evidence suggests that the early solar nebula disk formed in a stellar cluster, not far from a massive star (Adams 2010; Bergin et al. 2024; Desch & Miret-Roig 2024).

Massive OB-type stars release intense UV radiation, reaching the disk population that gradually emerges from the natal cloud (e.g., van Terwisga & Hacar 2023). Extreme-UV (EUV; $13.6 < E < 100$ eV) photons ionize the photoevaporative wind, creating the characteristic ionization front teardrop morphology around proplyds (e.g., O'dell et al. 1993; Bally et al. 2000; Maucó et al. 2023; Aru et al. 2024). External far-UV (FUV; $6 < E < 13.6$ eV) photons penetrate deeper into the disk, heating the gas and dust and altering its chemical composition by ionizing atoms with low ionization potential (IP), triggering the formation of molecular ions and radicals (e.g., Berné et al. 2023, 2024; Zannese et al. 2024, 2025), and desorbing ice grain mantles (e.g., Walsh et al. 2013; Goicoechea et al. 2024). This FUV-irradiated disk zone, a "photodissociation region" (PDR, e.g., Hollenbach & Tielens 1999) exhibits high ionization fractions ($x_e = n(e^-)/n_H$), a fundamental parameter in disk chemistry and dynamics, with x_e of a few 10^{-4} at the PDR edge if $x_e \approx x_{C^+}$. Cosmic rays have a greater penetration depth. They are responsible for the much lower, but somewhat uncertain, ionization fraction in the FUV-shielded disk midplane, with $x_e \propto \sqrt{\zeta/n_H}$ down to $\approx 10^{-11}$, where ζ is the H_2 ionization rate. Here, we assume that ζ is dominated by cosmic-ray ionizations, though it may also have local contributions from stellar X-rays and the decay of short-lived radionuclides (e.g., Cleeves et al. 2013, 2015).

Identifying tracers of FUV, x_e, and ζ in various regions of a protoplanetary disk is critically important. Since its detection in the interstellar medium (ISM) of our galaxy (Geballe & Oka 1996) and beyond (Geballe et al. 2006), the IR "absorption" spectrum

⋆ Corresponding author: javier.r.goicoechea@csic.es

of H_3^+ is considered one of the cleanest probes of ζ (e.g., McCall et al. 2002; Goto et al. 2008; Indriolo & McCall 2012). In ISM clouds, cosmic-ray ionization of H_2 produces H_2^+, which rapidly reacts with molecular hydrogen to form H_3^+,

$$H_2^+ + H_2 \rightarrow H_3^+ + H. \quad (1)$$

This is a highly exothermic reaction, ~1.7 eV (~20 000 K), nearly insensitive to the initial vibrational state of H_2^+ for excitation energies below ~1 eV (del Mazo-Sevillano et al. 2024). Depending on x_e, the destruction of H_3^+ can be dominated either by dissociative recombination with electrons or by exothermic proton transfer reactions with abundant species such as CO, N_2, and O (e.g., Herbst & Klemperer 1973; Watson 1973; Black & Dalgarno 1977). The likely detection[1] of infrared (IR) H_3^+ "emission" (see Schroetter et al. 2025b) in the irradiated disk d203-506, in the line of sight toward the Orion Bar, raises the question of whether ζ is enhanced in disks within clustered star-forming regions or whether alternative mechanisms contribute to H_3^+ formation.

In contrast to interstellar absorption measurements, H_3^+ emission has been detected in Jupiter's ionosphere through observations of its $\nu_2 = 2 \rightarrow 0$ overtone at ~2 μm (Drossart et al. 1989) and its fundamental $\nu_2 = 1 \rightarrow 0$ band at ~3.4–4.4 μm (Oka & Geballe 1990). The detection of H_3^+ emission in Jupiter, Saturn (Geballe et al. 1993), Uranus (Trafton et al. 1993), and Neptune (Melin et al. 2025) probes solar wind-driven ionospheric and auroral activity. The main source of H_2 ionization in planetary ionospheres is high-energy electron impacts, $H_2 + e^{-*} \rightarrow H_2^+ + 2e^-$, with some contribution from ionization by solar EUV radiation (e.g., Miller et al. 2000, 2020).

H_3^+ line emission outside the Solar System was first (tentatively) reported in the ejecta of Supernova 1987A (Tennyson & Miller 1994; Lepp & Dalgarno 1991) and in the disk around the Herbig Ae/Be star HD 141569 (Brittain & Rettig 2002). The later detection was disputed by Goto et al. (2005), who did not find any H_3^+ lines in follow-up observations. Until now, the most robust detection of interstellar H_3^+ $\nu_2 = 1 \rightarrow 0$ emission has come from JWST observations of ultraluminous IR galaxies (ULIRGs, Pereira-Santaella et al. 2024). The detection of ro-vibrational emission raises questions about H_3^+ formation and excitation mechanisms (collisional, radiative, or formation pumping; see e.g., Anicich & Futrell 1984; Le Bourlot et al. 2024).

A key feature of dense FUV-irradiated gas is the presence of significant quantities of thermal and FUV-pumped rotationally and vibrationally excited[2] H_2, hereafter H_2^*, which is typically much more chemically reactive than $H_2(v=0, J=0)$, the dominant form of H_2 in cold interstellar gas (Stecher & Williams 1972; Freeman & Williams 1982; Tielens & Hollenbach 1985; Sternberg & Dalgarno 1995; Agúndez et al. 2010). In PDRs, H_2^* initiates a "hot" chemistry, whereby endoergic reactions (endothermic or with activation energy barriers) become active and proceed rapidly. This "state-dependent" chemistry in disks remains poorly characterized (e.g., Walsh et al. 2013; Ruaud 2021), as few reaction rates are known and advanced computational methods are required to determine these rate constants (e.g., Zanchet et al. 2013a,b, 2019; Veselinova et al. 2021; Goicoechea & Roncero 2022). In this study we investigate the chemical pathways through which strong FUV radiation fields trigger the formation of abundant H_3^+ via a few specific reactions involving H_2^*. We theoretically investigate two fundamental reactions: $H_2(v'') + H^+ \leftrightarrow H_2^+(v') + H$, which is very endoergic in the left to right direction when $v'' < 4$ (by ~21 200 K when $v''=0$), and reaction $H_2(v'') + HOC^+ \rightarrow H_3^+(v') + CO$, which is endoergic by ~1500 K when $v''=0$ and $J''=0$ (see Appendices). Using detailed dynamical computations, we determine their vibrational-state dependent rate constants and incorporate them into our model simulating the PDR component of d203-506. In addition, we investigate the role of FUV-photoionization of $H_2^*(v \geq 4)$ (Ford et al. 1975), another state-dependent process that leads to the formation of H_2^+, and consequently H_3^+.

In Sect. 2, we summarize the most relevant properties of d203-506. In Sect. 3, we present our reference model of the disk's PDR component. In Sect. 4, we dissect this component into three zones and study the dominant chemical formation pathways for H_3^+ in these zones. In Sect. 5, we present and discuss our photochemical and excitation models.

2. The irradiated disk d203-506 and its H_3^+ emission

The disk d203-506 was first detected in silhouette against the optical background of the Orion Nebula by *Hubble* (Bally et al. 2000) and later in HCO^+ by ALMA (Champion et al. 2017). More recent observations from the Keck Observatory, Very Large Telescope (VLT), and *James Webb* Space Telescope (JWST) have revealed the extended nature of its PDR component – the irradiated outer disk surface and photoevaporative wind – created by FUV radiation from θ^1 Ori C, the most massive O-type star in the Trapezium (Berné et al. 2023, 2024; Haworth et al. 2023; Habart et al. 2024; Goicoechea et al. 2024; Zannese et al. 2024, 2025).

While the exact position (in the line of sight) of d203-506 is uncertain (e.g., Haworth et al. 2023), the Orion Nebula Cluster lies at a distance of ~400 pc (e.g., Kounkel et al. 2018). Berné et al. (2024) determined the mass of the host star (~0.3 $M_\odot$), and the disk's mass (~ 10 $M_{Jup} \simeq 10^{-2}$ $M_\odot$) and radius (~100 au ≃ 0.25″). The estimated flux of the external FUV field, derived from near-IR fluorescent OI and CI emission lines, is $G_0 \simeq 2{\times}10^4$ (Berné et al. 2024; Goicoechea et al. 2024), where G_0 is the mean interstellar FUV field in Habing units ($G_0 = 1$ is equal to $1.6{\times}10^{-3}$ erg cm^{-2} s^{-1}; Habing 1968). In addition, d203-506 exhibits shock-excited gas from a small jet (HH 520), observed in [Fe II] (Haworth et al. 2023; Berné et al. 2024). Most molecules exhibiting extended emission in the disk's PDR show their peak near a bright "spot" facing the Trapezium (Berné et al. 2024), which likely corresponds to a column density enhancement, perhaps the interaction region between the PDR and the jet.

This disk is particularly interesting for constraining the effects of FUV radiation, as it does not exhibit ionization fronts produced by EUV radiation (Haworth et al. 2023). In addition, the nearly edge-on orientation of d203-506, with an estimated inclination of $i > 75°$ (based on the non-detection of the internal star; Berné et al. 2024), makes it an excellent target for studying the vertical effects of FUV radiation in the upper disk and neutral wind. This geometry allows for the PDR component to be isolated more easily, since the very high dust optical depth at short wavelengths renders IR observations insensitive to the cold disk midplane and inner disk.

[1] Although H_3^+ possesses equilateral triangle symmetry, and therefore lacks a permanent dipole, its vibrational modes can break this symmetry, leading to strong dipole-induced transitions (e.g., Tennyson & Miller 1994; Miller et al. 2020). The only fully allowed transition is the infrared-active asymmetric stretch-bend mode ν_2, with a band origin at 2,521.6 cm^{-1} (~4 μm), first observed in the laboratory by Oka (1980).

[2] Berné et al. (2024) reported the detection of IR H_2 lines up to $v=4$ originating from the PDR component of d203-506. They also detected highly excited rotational lines of $H_2(v=0)$ up to $J=17$. Higher spectral resolution observations of interstellar PDRs such as the Orion Bar show H_2 lines in vibrationally excited levels up to $v=12$ (Kaplan et al. 2021).

Schroetter et al. (2025b) reported the likely detection of several H_3^+ emission lines of the $\nu_2 = 1 \rightarrow 0$ band, including the $R(1,0)$, $Q(1,0)$, $Q(5,G)$, $R(7,0)$, and $R(7,6)^u$ lines[3]. The higher excitation lines are not detected in the ISM of galaxies (Pereira-Santaella et al. 2024) and suggest higher excitation conditions in d203-506. Although clearly visible in the stacked spectrum, the reported lines are faint and close to the detection limit, leaving the presence of H_3^+ emission in d203-506 open to interpretation.

3. Representative model of the externally irradiated outer disk and photoevaporative wind

To guide our interpretation of the H_3^+ emission in externally irradiated disks, we first present a representative model of their PDR component, its structure, and physical conditions. We assume that at the physical scales probed by JWST, the density distribution is smooth across the inner neutral wind and outer disk surface. Thus, as a first approximation, we adopted a constant density model. We simulated the disk PDR as a 1D stationary slab of gas and dust using an enhanced version of the Meudon PDR[4] code v7.0 (Le Petit et al. 2006). Since we were focusing on d203-506, we adopted $G_0 = 2{\times}10^4$ and $\zeta = 10^{-16}$ s^{-1} (Berné et al. 2024). Our model solves the λ-dependent attenuation of FUV photons ($\lambda < 912$ Å), considering dust extinction and line self-shielding. We treat the λ-dependent absorption and anisotropic scattering of FUV photons by dust grains that follow a uniform size distribution $\propto a^{-3.5}$ (Mathis et al. 1977), with $a_{\rm min} = 0.02$ μm and $a_{\rm max} = 1$ μm as the minimum and maximum grain radii (for details, see Goicoechea & Le Bourlot 2007). This choice provides a total-to-selective extinction ratio of $R_V \simeq 5.9$ and a dust extinction cross section $\sigma^{\rm d}_{\rm ext} = 7 \times 10^{-22}$ cm^2 H^{-1} at 1000 Å (absorption plus scattering). While these grains are bigger than ISM grains (where $\sigma^{\rm d}_{\rm ext}$ is ~3 times larger), they reflect the modest grain growth expected in the upper layers of young irradiated disks (e.g., Störzer & Hollenbach 1999; Birnstiel et al. 2018).

Our detailed treatment of the penetration of FUV radiation, multilevel H_2 excitation (up to $v = 14$), thermal balance, and chemistry allows for the precise determination of the H/H_2 and C^+/C/CO transition layers, which is crucial for understanding the origin of the H_3^+ emission. In order to account for the formation of the outer water snow line, the model includes gas-phase chemistry and simple grain surface chemistry for O, OH, H_2O, O_2, and CO ice mantles (see Putaud et al. 2019; Goicoechea et al. 2021). However, we do not model the different reactivities of *ortho*- and *para*-H_2 or H_3^+, nor do we compute the vibrational populations of chemical reaction products. In addition, we neglect the wind dynamics (see e.g., Haworth & Owen 2020).

Based on JWST studies of d203-506, we adopted a gas density $n_{\rm H} = n({\rm H}) + 2n(H_2) = 10^7$ cm^{-3} for its PDR component (Berné et al. 2024; Goicoechea et al. 2024; Zannese et al. 2024, 2025). Figure 1 dissects the physical structure of the PDR as a function of depth (along the external illumination direction and in magnitudes of visual extinction, A_V), roughly representing the vertical structure of the outer disk and wind. This figure shows the decreasing gas temperature and increasing H_2 density from the PDR edge to the more FUV-shielded disk interior. Figure 2 shows the FUV radiation field (in energy density) at different zones of the disk PDR (in A_V). In this plot, we only show the high-energy FUV photon range from 13.6 to 12.6 eV relevant to H_2^* photoionization.

[3] The NIR spectrum of this disk is very rich and additional H_3^+ lines remain blended with lines of other species (Schroetter et al. 2025b).
[4] https://pdr.obspm.fr/pdr_download.html

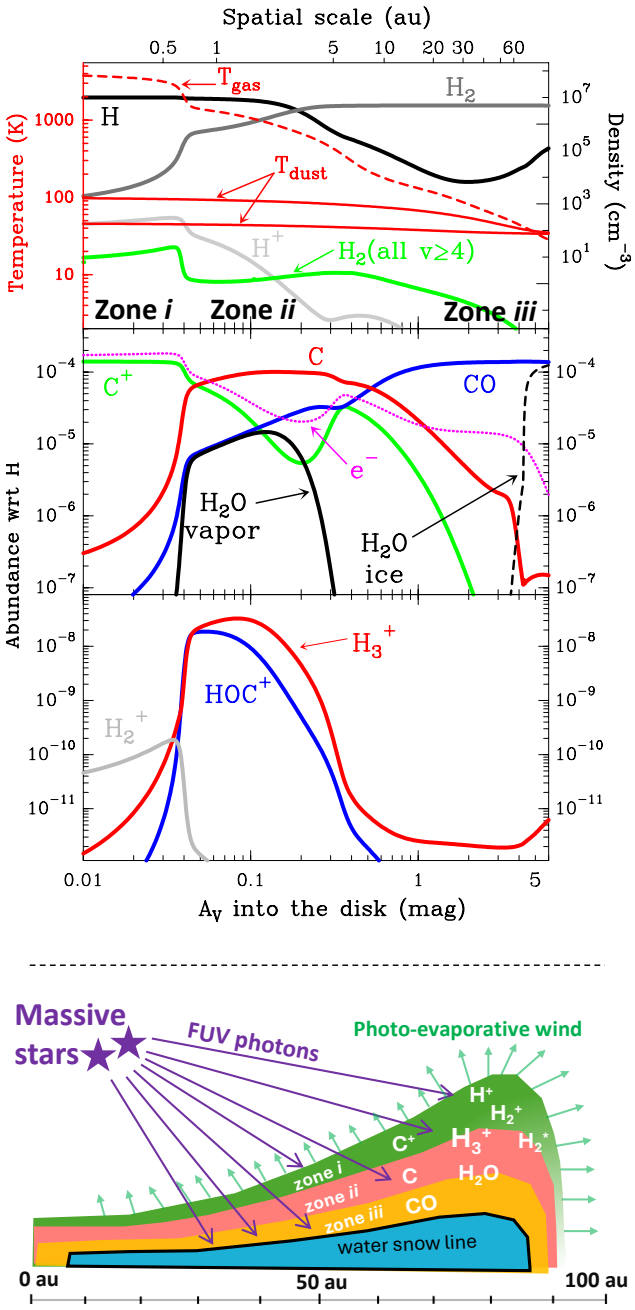

Fig. 1. Physical (approximately vertical) structure of d203-506. *Upper panel*: model profiles of gas density, gas temperature, and $a^{-3.5}$ grain-size distribution, showing the highest and lowest dust temperatures (corresponding to $a_{\rm min}$ and $a_{\rm max}$ grain radii, respectively) as a function of depth into the PDR. The green curve shows the density of $H_2^*(v \geq 4)$. *Lower panels*: abundance profiles of selected species. *Bottom sketch*: simplified sketch illustrating the PDR component of an externally irradiated protoplanetary disk. The different colored regions correspond to the chemical zones discussed in Sect. 4.

Owing to the low $G_0/n_{\rm H}$ ratio, the FUV spectrum is significantly blanketed by H_2 absorption lines (Fig. 2).

H_2 molecules are photodissociated at the very surface of the PDR ($A_V \lesssim 0.2$ mag). In these hot and predominantly atomic gas layers, the abundance of H atoms exceeds that of H_2. That is, $x({\rm H}) > x(H_2)$ and $f(H_2) = 2n(H_2)/n_{\rm H} < 2/3$, where $f(H_2)$ is the molecular gas fraction. Owing to the high densities and temperatures, the excited rotational levels of $H_2(v = 0)$ become

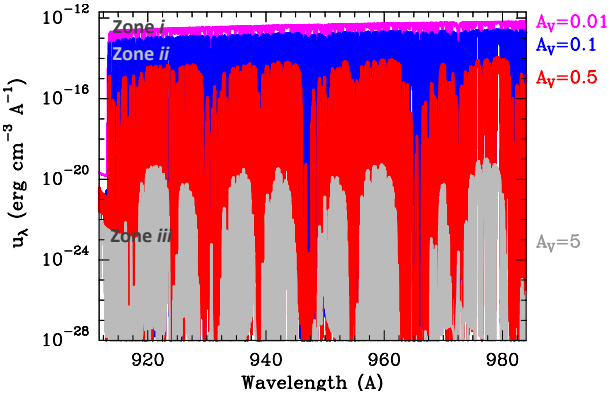

Fig. 2. Predicted λ-dependent FUV radiation field at different depth positions from the PDR surface into the disk. We show the local FUV energy density in units of erg cm^{-3} Å^{-1}, from the Lyman cut to 12.6 eV.

significantly populated by inelastic collisions, with $T_{\rm rot} \approx T_{\rm gas}$. Due to the de-excitation of FUV-pumped H_2 electronic levels (Lyman and Werner bands), a significant fraction of the existing H_2 resides in excited vibrational states too ($v > 0$; see the upper panel of Fig. 1). Specifically, the predicted fractional abundance of H_2^* molecules in vibrational states $v \geq 4$ (relative to those in the ground state) reaches $\sim 1\%$ (this fraction increases for lower gas densities, see specific models in Appendix A). A key feature of PDRs is that the enhanced abundance of H_2^* significantly impacts the chemistry and the position[5] of the C^+/C/CO transition layers. Owing to self-shielding and a reduced FUV flux, H_2 becomes more abundant than H at $A_V > 0.2$ mag. This marks the so-called "dissociation front", where $n(H) \simeq n(H_2)$. Most of the IR molecular emission detected by JWST in d203-506 originates from these warm disk layers, where we predict $T_{\rm gas} \approx 1000$ K, in agreement with the observed H_2 rotational temperatures (Berné et al. 2024). The lowest panel of Fig. 1 shows a simplified sketch illustrating three zones of the disk PDR (from the outside to the inside): predominantly atomic hot gas at the neutral wind edge (zone *i*), warm gas near the H/H_2 dissociation front (zone *ii*), and colder, partially FUV-shielded disk gas (zone *iii*). These zones also correspond to different regimes of the H_3^+ chemistry.

4. H_3^+ chemistry in three different disk regions

In this section, we introduce the main sources of H_2 ionization and the dominant pathways leading to H_3^+ in the three distinct zones of the disk PDR (Fig. 1). This analysis is based on the dominant H_3^+ formation and destruction mechanisms predicted by our reference model of d203-506 across the disk PDR (see the chemical networks in Figure 3).

4.1. Zone i: Predominantly atomic PDR gas

This thin outermost zone ($A_V < 0.03$ mag, less than one astronomical unit, au) is exposed to the nearly unshielded external FUV field and is characterized by very high temperatures ($\simeq 3000$ K in this model), fairly low $f(H_2)$, and significant relative abundances

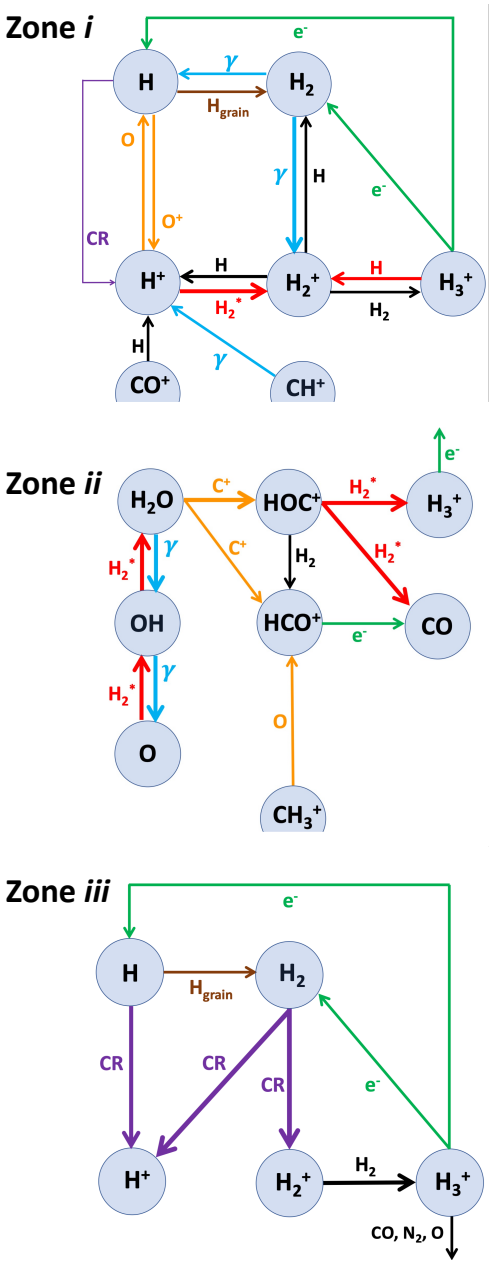

Fig. 3. Dominant H_3^+ formation and destruction pathways in different zones of a strongly irradiated protoplanetary disk (see Fig. 1). A thicker arrow represents a dominant chemical pathway. Red arrows show endoergic reactions. These reactions become fast at high $T_{\rm gas}$ and where significant H_2^* exists. "CR" refers to ionization caused by cosmic rays and "γ" refers to FUV photons. Orange arrows represent ion-molecule and charge exchange reactions. Green arrows represent dissociative recombinations with electrons. Incomplete circles indicate that these are not the starting points of the chemistries.

of H_2^*. The dominant H_2 ionization pathway is the reaction

$$H_2(v'') + H^+ \rightarrow H_2^+(v') + H, \quad (2)$$

where v'' and v' denote the vibrational levels of the reactant and product molecules, respectively, in their ground electronic state. This process – both charge transfer (CT) and reactive charge transfer (RCT) – is very endoergic, by about 1.83 eV $\simeq$21 200 K, when $v'' = 0$ (Ichihara et al. 2000; Krstić et al. 2002; Plasil et al. 2012; Sanz-Sanz et al. 2021). Thus, it is a negligible process in cold

[5] H_2^* readily reacts with C^+ and O to form abundant CH^+ and OH (as observed in d203-506; Zannese et al. 2024, 2025). These reactions are highly endoergic when H_2 ($v = 0$, $J = 0$), but they become fast at high $T_{\rm gas}$ and when H_2^* is available, even shifting the C^+/C transition ahead of the H/H_2 dissociation front (see Fig. 1) and triggering the formation of specific molecular species in the PDR.

Table 1. Rate constants discussed in this work.

Reaction	α ($cm^3\ s^{-1}$)	β	γ (K)
$H_2(v{=}0) + H^+ \rightarrow H_2^+ + H$	2.70e−10		22 000
$H_2(v{=}1) + H^+ \rightarrow H_2^+ + H$	4.00e−10		16 500
$H_2(v{=}2) + H^+ \rightarrow H_2^+ + H$	3.20e−10		10 500
$H_2(v{=}3) + H^+ \rightarrow H_2^+ + H$	5.74e−11	+0.76	4254
$H_2(v{=}4) + H^+ \rightarrow H_2^+ + H$	3.74e−10	+0.75	−126
$H_2(v{=}5) + H^+ \rightarrow H_2^+ + H$	2.28e−10	+0.77	−182
$H_2(v{=}6) + H^+ \rightarrow H_2^+ + H$	7.58e−10	+0.37	−92
$H_2(\text{thermal}) + H^+ \rightarrow H_2^+ + H$	1.32e−09	+0.42	21 993
$H_2^+ + H \rightarrow H_2 + H^+$	6.64e−10	+0.21	−2.0
$HOC^+ + H_2(v{=}0) \rightarrow H_3^+ + CO$	1.25e−11	+1.07	−80.5
$HOC^+ + H_2(v{=}1) \rightarrow H_3^+ + CO$	3.44e−10	+0.06	3.4
$HOC^+ + H_2(v{=}2) \rightarrow H_3^+ + CO$	4.77e−10	−0.01	7.1
$HOC^+ + H_2(v{=}3) \rightarrow H_3^+ + CO$	5.34e−10	−0.01	−1.9
$HOC^+ + H_2(v{=}4) \rightarrow H_3^+ + CO$	5.40e−10	+0.01	−12.2
$HOC^+ + H_2(v{=}0) \rightarrow HCO^+ + H_2$	2.37e−10	−0.37	20.0
$HOC^+ + H_2(v{=}1) \rightarrow HCO^+ + H_2$	2.16e−10	−0.35	20.0
$HOC^+ + H_2(v{=}2) \rightarrow HCO^+ + H_2$	1.66e−10	−0.33	20.0
$HOC^+ + H_2(v{=}3) \rightarrow HCO^+ + H_2$	1.47e−10	−0.37	20.0
$HOC^+ + H_2(v{=}4) \rightarrow HCO^+ + H_2$	1.19e−10	−0.29	20.0
$HOC^+ + H \rightarrow CO^+ + H_2$	5.10e−10		7125
$HCO^+ + H \rightarrow CO^+ + H_2$	1.30e−09		24 500
$H_3^+ + H \rightarrow H_2^+ + H_2$	2.10e−09		20 000

Notes. Rate constants from fitting the Arrhenius-like form $k(T) = \alpha\,(T/300\,\text{K})^{\beta}\exp(-\gamma/T)$ to reaction rates computed in this study, and valid in the $T \simeq 100$–2000 K range. For the last three endoergic reactions, see footnote 10.

molecular gas. However, it becomes accessible at high temperatures ($T_{\rm gas} > 1000$ K) and as higher v'' levels of H_2^* are populated by de-excitation of FUV-pumped H_2. In Appendix B we describe the quantum dynamical methods we used to calculate accurate vibrational-state dependent rate constants for reaction (2). Table 1 summarizes the derived v''-state specific rate constants as well as the thermal[6] rate, derived from these constants, in the form of Arrhenius-like fits. For $H_2(v'')$ in low vibrational states ($v'' < 4$) and at warm to cold gas temperatures ($T_{\rm gas} < 1000$ K), the reaction (2) is extremely slow (see Fig. 4). However, for $v'' \geq 4$ and for $T_{\rm gas} > 1000$ K, the CT reaction becomes energetically accessible and the reaction rate much faster.

[6] To distinguish between the role of high gas temperatures and the effect of nonthermal populations of FUV-pumped $H_2^*(v'')$ on the chemistry, it is useful to determine the thermal rate constants. These are Boltzmann averages of the individual v''-state-specific rate constants, defined as

$$k_{\rm th}(T) = \frac{\sum_{v''=0}^{14} k_{v''}(T)\, e^{-E_{v''}/k_{\rm B}T}}{\sum_{v''=0}^{14} e^{-E_{v''}/k_{\rm B}T}}. \quad (3)$$

Figure 4 shows the resulting thermal rates for reaction (2) as a dashed black curve. At low temperatures ($T_{\rm gas} \ll E_{v''}\,(H_2)/k_B$), as in most applications involving cold molecular gas, the thermal rate is roughly that of $H_2(v''=0)$. That is, $k_{\rm th}(T) \simeq k_{v''=0}(T)$ (e.g., Agúndez et al. 2010). In the case of reaction (2), $k_{\rm th}$ is significantly larger than $k_{v''=0}$ because the rate constants increase by orders of magnitude when H_2 is vibrationally excited. For reaction (9), the differences between $k_{v''=0}$ and $k_{v''\geq 1}$ are not that large, and $k_{\rm th}$ becomes slightly higher than $k_{v''=0}$ at high temperatures, where the vibrationally excited levels start to be populated.

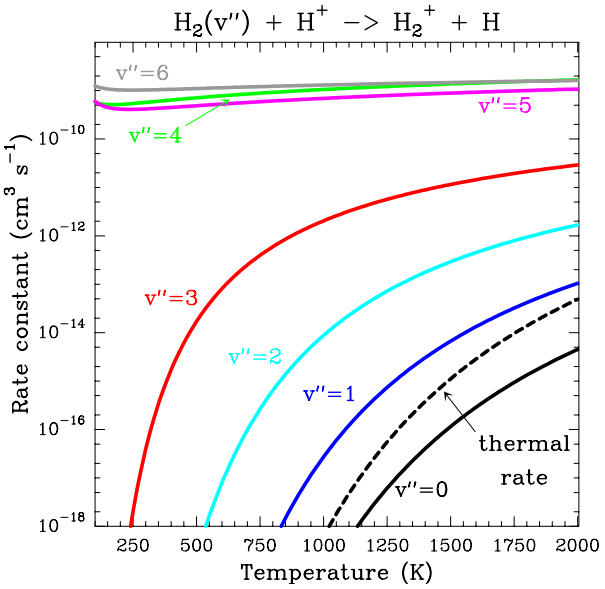

Fig. 4. Calculated vibrational-state-specific rate constants of reaction $H_2(v'') + H^+ \rightarrow H_2^+ + H$ (reaction (2)). The dashed curve represents the thermal[6] rate constant determined from thermal averages of these constants.

Given that H_3^+ formation via cosmic-ray ionization of H_2 is negligible in this zone, the central question becomes how hydrogen atoms are ionized. A fraction of H atoms are directly ionized by cosmic rays. In addition, the photodissociation of CH^+ and reactions of CO^+ with H atoms become significant "chemical sources" of H^+ in high-G_0 environments. These reactive molecular ions[7] are natural products of PDR chemistry (e.g., Sternberg & Dalgarno 1995) and readily form as $T_{\rm gas}$ and the H_2^* abundance increase in the disk PDR.

In this zone, H^+ ions are destroyed by reactions with O atoms,

$$H^+ + O(^3P_J) \rightarrow H + O^+. \quad (4)$$

This resonant CT is endoergic[8] when the oxygen atom is the ground fine-structure state ($J = 2$) (Chambaud et al. 1980; Stancil et al. 1999; Spirko et al. 2003), with a rate constant $\propto \exp(-230\,\text{K}/T_{\rm gas})$. Thus, it is much faster at high $T_{\rm gas}$, so that H^+ ions follow reaction (4) instead of recombining with electrons. Still, a small fraction of H^+ ions forms H_2^+ through reaction (2). The inverse CT of reaction (4) ($H + O^+$) is exothermic and quickly returns most of the charge to H^+.

Although FUV photons (below the Lyman limit) cannot ionize molecular hydrogen when H_2 is in its lowest vibrational states (as IP(H_2) = 15.43 eV or 124,417.491 cm^{-1}; Liu et al. 2009), H_2^* molecules in $v'' \geq 4$ can be ionized[9] by FUV radiation. That is,

$$H_2(v'' \geq 4) + \text{FUV} \rightarrow H_2^+(v') + e^-. \quad (5)$$

[7] Reactive ions such as H_2^+, CH^+, and HOC^+ are transient molecules for which the timescale of reactive collisions (leading to molecular destruction) is comparable to or shorter than that of inelastic collisions (e.g., Black 1998). Properly treating their molecular excitation usually requires incorporating chemical formation and destruction rates into the statistical equilibrium level equations (see Appendix E).

[8] We predict the following $O(^3P_J)$ fine-structure level populations in zones *i* and *ii*: ∼60 % in $J = 2$, ∼30 % in $J = 1$, and ∼10 % in $J = 0$. In zone *iii*, most of the oxygen is in the ground fine-structure level.

[9] The $H_2(v{=}4, J{=}0)$ level is at an energy of 1.89 eV (or 21504.7 cm^{-1}) above the ground state (e.g., Komasa et al. 2011). Thus, FUV photons with $E_\lambda = \text{IP}(H_2) - E_{H_2(v\geq 4)} < 13.6$ eV produce ionization and lead to H_2^+.

This is a FUV-driven source of H_2 ionization, and of electrons, that has not been considered in PDR models before. This mechanism is also a destruction process of H_2 levels with $v'' \geq 4$. We determined the role of H_2^* photoionization by considering the state-to-state photoionization cross sections, $\sigma_\lambda(v'') = \sum_{v'} \sigma_\lambda(v'' \rightarrow v')$, computed by Ford et al. (1975). These cross sections are on the order of $\sim 10^{-18}$ cm^{-2}, and require FUV photons with energies above 12.6 eV ($\lambda < 984$ Å, see Fig. 2). Appendix C describes the details of our calculations.

The photoionization rate of H_2^* from a given $v'' \geq 4$ level, $\kappa_{\rm phi}(H_2, v'')$, is given by

$$\kappa_{\rm phi}(H_2, v'') = \frac{1}{h} \int_{912}^{\lambda_t} \sigma_\lambda(v'')\, u_\lambda\, \lambda\, d\lambda \quad (s^{-1}), \tag{6}$$

where u_λ is the local energy density of the FUV radiation field (in erg cm^{-3} Å^{-1}) at a given disk position (see Fig. 2). Hence, the total H_2^+ formation rate due to $H_2^*(v''\geq 4)$ photoionization, $F_{\rm phi}(H_2^+)$, is given by

$$F_{\rm phi}(H_2^+) = \sum_{v''} n(H_2, v'')\, \kappa_{\rm phi}(H_2, v'') \quad (cm^{-3}\, s^{-1}), \tag{7}$$

where $n(H_2, v'')$ (in cm^{-3}) are the local $H_2^*(v'')$ level populations.

In zones *i* and *ii*, reaction (1) is not the dominant destruction pathway of H_2^+. Instead, owing to the high abundance of H atoms, the reverse process of reaction (2),

$$H_2^+(v'') + H \rightarrow H_2(v') + H^+, \tag{8}$$

is the dominant destruction pathway for H_2^+. This reaction is very exoergic, and has been investigated in the laboratory (Karpas et al. 1979) and by quantum dynamical methods (Sanz-Sanz et al. 2021). In Appendix B, we summarize how we determined the state-dependent rate constants for this reaction (CT and RCT) in the temperature range $T_{\rm gas} \simeq 100$–2000 K. Table 1 shows the computed thermal rate constant – independent of the vibrational state of H_2^+ (as we do not explicitly follow the excitation of H_2^+ molecules) – that we used in our models. Reactions of H_2^+ with H limit the formation of H_3^+ in FUV-irradiated gas with relatively low $f(H_2)$. In general, reactions involving H atoms can constitute an efficient destruction pathway for molecules at high temperatures because these processes are typically highly endoergic[10]. However, they only impact a thin layer at the PDR edge, where temperatures are very high and $x(H) \gg x(H_2)$.

4.2. Zone ii: molecular PDR gas

Figure 3 (middle panel) shows the gas-phase reactions leading to H_3^+ in zone *ii*, near the dissociation front (at $A_V \simeq 0.2$ mag in this reference model; Fig. 1). Because of its higher gas column density ($0.03 < A_V < 0.3$ mag, corresponding to a vertical scale of ~5–10 au) and elevated temperatures ($T_{\rm gas} \sim 1000$ K), zone *ii* is predicted to be the primary contributor to the observed H_3^+ column density in d203-506. Remarkably, the chemistry responsible for H_3^+ formation in this zone is largely independent of cosmic-ray ionization, but ultimately related with the presence of enhanced abundances of C^+ and water vapor in the outer disk surface. We find that H_3^+ forms mainly through reaction

$$H_2(v'') + HOC^+ \rightarrow H_3^+ + CO, \tag{9}$$

which is endoergic by ~1500 K when $v'' = 0$ (including zero-point energies, ZPEs, see Appendix D and Klippenstein et al. (2010)). These products have been observed in experiments at room temperature (e.g., Freeman et al. 1987). However, there is no evidence of H_3^+ formation at low temperatures (at least at 25 K; see Smith et al. 2002).

Reaction (9) competes with the isomerization reaction

$$H_2(v'') + HOC^+ \rightarrow HCO^+ + H_2, \tag{10}$$

which is exoergic (Smith et al. 2002). In Appendix D, we describe the ZPE-corrected quasi-classical trajectory dynamical methods we used to calculate the v''-state-dependent rate constants of reactions (9) and (10). Figure 5 show the resulting rates. We find that for $H_2(v''=0, J''=0)$ and for low gas temperatures ($T_{\rm gas} < 100$ K), the isomerization reaction (10) is the relevant channel. However, for H_2^*, and as $T_{\rm gas}$ increases, the channel leading to $H_3^+ + CO$ becomes increasingly relevant[11], and becomes the primary pathway for H_3^+ formation in this disk zone.

HOC^+ is the less stable isomer of the widespread HCO^+ cation. HOC^+ is a reactive molecular ion readily seen in interstellar PDRs (e.g., Ziurys & Apponi 1995; Fuente et al. 2003; Liszt et al. 2004; Savage & Ziurys 2004; Goicoechea et al. 2009, 2017). Its main formation pathway is the very exoergic reaction

$$C^+ + H_2O \rightarrow HOC^+/HCO^+ + H. \tag{11}$$

This reaction has been studied in the laboratory (Martinez et al. 2008; Yang et al. 2021), implying a branching ratio to HOC^+ of $\gtrsim 0.68$ because the formation of HCO^+ requires carbon insertion into the O–H bond, which is less likely (e.g., Ishikawa et al. 2001). Experimental studies suggest a reaction rate of $\gtrsim 10^{-9}$ cm^3 s^{-1} and

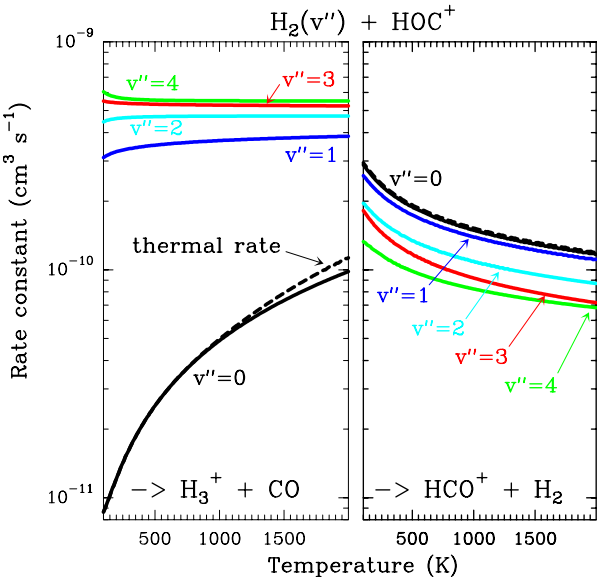

Fig. 5. Calculated H_2 vibrational-state-specific rate constants of reaction $H_2(v'') + HOC^+$ producing $H_3^+ + CO$ (left box) and $HCO^+ + H_2$ (right box). The dashed curves represent the thermal[6] rate constant determined from thermal averages of the state-dependent rates.

[10] Our chemical network includes endoergic reactions of H atoms with H_3^+, HCO^+, HOC^+ (Table 1), and other molecules. If the forward rate is not known, we adopt the rate constant of the reverse reaction multiplied by $e^{-\Delta E/T}$, where ΔE is the endothermicity of the forward reaction (see e.g., Pineau des Forets et al. 1986).

[11] Reaction (9) becomes exoergic for H_2^* in $v'' = 0$ and $J'' \geq 4$.

a slight inverse temperature dependence (Martinez et al. 2008; Yang et al. 2021). Therefore, the formation of abundant HOC^+ (and thus H_3^+) in the disk's PDR is directly linked to the presence of FUV photons, which can ionize C atoms, and to the existence of abundant water vapor, enabled by elevated gas temperatures.

Figure 3 (middle panel) shows the endoergic gas-phase reactions that lead to the formation of H_2O at warm temperatures. The initial step involves the formation of the OH radical,

$$O + H_2(v'') \rightarrow OH(v') + H. \quad (12)$$

This reaction is endoergic by $E/k \sim 770$ K and has an activation barrier of $E_a/k \sim 6900$ K from $H_2(v{=}0)$ (Veselinova et al. 2021). The second step is reaction

$$OH + H_2(v'') \rightarrow H_2O + H, \quad (13)$$

which is exoergic, but has a barrier[12] of a few thousand Kelvin. Thus, high T_{gas} conditions, and the presence of H_2^*, lead to water vapor in this PDR zone. All in all, the strong external FUV radiation initiates a cycle of H_2O formation, photodissociation, and reformation. This cycle has been observationally confirmed by the detection of rotationally hot OH – the signature of H_2O photodissociation – and of vibrationally excited OH – the signature of reaction (12) – in d203-506 (Zannese et al. 2024).

4.3. Zone iii: Partially FUV-shielded molecular gas

Figure 3 (lower panel) shows the dominant gas-phase reactions leading to H_3^+ in FUV-shielded (or low illumination) molecular gas, where $A_V \gtrsim 5$ mag. The initial step involves cosmic-ray ionization of H_2:

$$H_2 + CR \rightarrow H_2^+ + e^- + CR'. \quad (14)$$

This is the "standard" chemistry of interstellar clouds with $f(H_2) \rightarrow 1$ (e.g., Dalgarno 2006). In steady state, the density of H_3^+ molecules is simply given by

$$n(H_3^+) \simeq \frac{\zeta\, n(H_2)}{\alpha_e\, n(e) + \sum_X k_x\, n(X)}, \quad (15)$$

where we consider H_3^+ formation through reaction (1) and H_3^+ destruction through dissociative recombinations with electrons (with a rate constant $\alpha_e \sim T^{-0.5}$) and proton transfer reactions with X = CO, N_2, O, and so on, with a rate constant, k_x. We note that this expression is independent of the rate constant of reaction (1). In FUV-shielded dense molecular gas, n(e) is typically low, $\alpha_e\, n(e) \ll \sum_x k_x\, n(x)$, and $x(H_3^+)$ is proportional to ζ. This regime dominates deeper inside the cold midplane ($T_{gas} < 100$ K), but results in lower local H_3^+ abundances – $x(H_3^+)$ of several 10^{-11} for $\zeta = 10^{-16}$ s^{-1} (or several 10^{-12} if $\zeta = 10^{-17}$ s^{-1}) – compared to the PDR, where H_3^+ abundances are typically several 10^{-8}.

5. Discussion

Here, we analyze and discuss our H_3^+ photochemical and excitation models, along with the sensitivity of the results to variations in the external radiation field and the cosmic-ray ionization rate.

[12] Since state-dependent rate constants, $k_{v,J}(T_{gas})$, do not exist for reaction (13), we modeled them by adopting state-dependent rate constants where the energy $E_{v,J}$ of each H_2^* ro-vibrational state is subtracted from the reaction barrier ΔE (when $\Delta E > E_{v,J}$).

5.1. Photochemical model results

Figure 6 (left panel, upper box) shows the predicted distribution of H_2 abundances (relative to the total H_2 density) across various rotationally and vibrationally excited H_2 levels as a function of depth into the disk. The lower box shows the resulting H_2^+, H_3^+, and HOC^+ abundance profiles. In this box, continuous curves show the results from models that use the specific state-dependent rate constants for reactions (2), (9), (10), and for photoionization of $H_2(v''{\geq}4)$. This represents our complete reference model of d203-506. The dotted curves correspond to models that neglect $H_2(v''{\geq}4)$ photoionization, which we find to play a minor role at the high gas densities considered. However, this process plays a more dominant role at lower densities due to the more nonthermal relative populations of FUV-pumped $H_2(v'' \geq 4)$ levels (see models in Appendix A). Dashed curves correspond to models neglecting H_2 photoionization and using the thermal rate constants computed from the state-to-state rates. Again, this approximation is sufficiently accurate for $n_H = 10^7$ cm^{-3}, but becomes much less reliable in lower-density gas (see Fig. A.2).

The right panels of Fig. 6 show the formation rate of H_2^+ from different reactions (upper box), as well as the percentage contribution of different reactions to the total H_3^+ formation rate (lower box). In the predominantly atomic PDR (zone *i*), H_3^+ formation is dominated by the reaction $H_2 + H_2^+$, but the primary formation pathway for H_2^+ is the reaction $H_2 + H^+$ – with a significant supply of H^+ from (photo)chemical reactions – along with a minor contribution from the photoionization of H_2^* ($v \geq 4$). The resulting H_3^+ abundance in zone *i* is not very high because destruction reactions with H atoms and dissociative recombinations with electrons are both very efficient. In terms of local abundances, this thin zone is characterized by $x(H^+) \simeq$ a few $10^{-5} \gg x(H_2^+) \gtrsim x(H_3^+) \simeq 10^{-12}$. This further implies that, even in the absence of an ionization front, narrow hydrogen recombination lines could still trace the neutral PDR (see observations by Boyden et al. 2025).

Near the H/H_2 dissociation front (disk zone *ii*), H_3^+ reaches its peak abundance ($\sim 3{\times}10^{-8}$) and column density ($\simeq 8.5 \times 10^{12}$ cm^{-2}). The $x(H_3^+)$ profile closely follows that of HOC^+ and, consequently, that of water vapor, which locally reaches very high abundances, $x(H_2O) \sim 10^{-5}$, due to the high gas temperatures and the efficiency of reactions (12) and (13) in converting atomic oxygen into H_2O. At the $x(H_3^+)$ peak, H_3^+ formation is driven almost exclusively by $H_2 + HOC^+$ reactions. In our model, the majority of the H_3^+ column density originates from this zone. Its formation is largely independent of cosmic-ray ionization and instead depends on the abundance of HOC^+. Indeed, the observed distribution of HCO^+ $J = 4$–3 emission in d203-506 – matching that of vibrationally excited H_2^* (Berné et al. 2024), highly rotationally excited OH (i.e., the product of water vapor photodissociation; Zannese et al. 2024), and fluorescent C I emission (Goicoechea et al. 2024) – implies that HOC^+, and thus H_3^+, originate from this PDR component.

In the more FUV-shielded and colder molecular gas, where $f(H_2) \rightarrow 1$ (disk zone *iii*), most gas-phase carbon becomes locked in CO. As the gas temperature and FUV flux decrease, conditions begin to favor the formation of abundant water ice mantles. Consequently, the gaseous C/O abundance ratio increases. Owing to strong external irradiation – leading to ice-mantle photodesorption and dust grain heating – the vertical position of the water snow line is shifted deeper inward (e.g., Goicoechea et al. 2024) compared to that in isolated disks (e.g., Öberg et al. 2011; Öberg & Bergin 2016). In terms of the ionization fraction, $x(H^+)$ and $x(e^-)$ decrease drastically in this

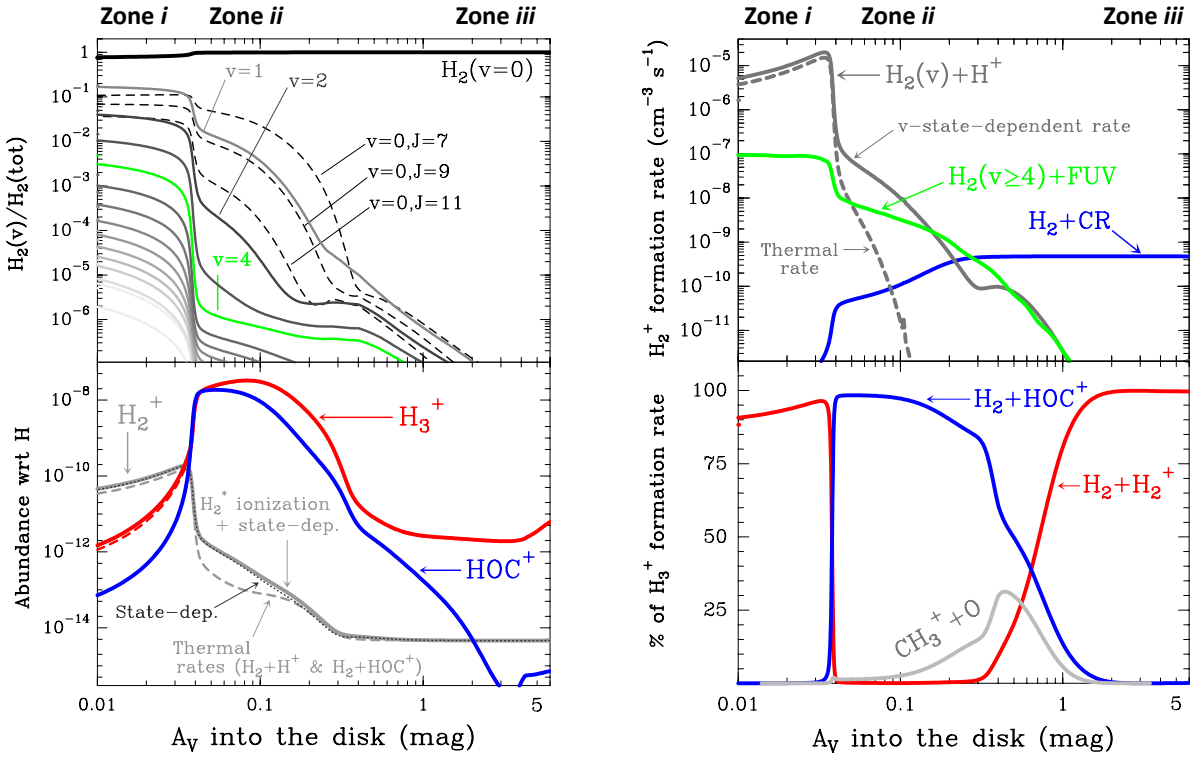

Fig. 6. Models of the PDR component in d203-506. *Left panels*: H_2 relative populations and abundances. The upper panel shows the normalized distribution of $H_2(v)$ populations across different vibrational levels (solid curves), along with the rotationally excited $H_2(v=0, J=7, 9, 11)$ levels (dashed curves). The lower panel displays abundance profiles of H_2^+, H_3^+, and HOC^+. Continuous curves show results for models using state-dependent rate constants for reactions (2), (9), (10), and for $H_2(v\geq4)$ photoionization (the complete reference model). Dotted curves are for models neglecting H_2 photoionization. Dashed curves are for models neglecting H_2 photoionization and using the thermal rate constants for reactions (2), (9), and (10). *Right panels*: chemical formation rates. H_2^+ formation rates as a function of depth into the PDR (upper box). Contribution (in %) to the H_3^+ formation rate as a function of depth into the PDR (lower box).

zone. Here, cosmic rays, X-rays, and perhaps the decay of short-lived radionuclides become the only significant sources of ionization (Cleeves et al. 2013, 2015). H_3^+ forms through reactions between H_2 and H_2^+. However, the local H_3^+ abundances are lower – approximately 10^{-11} for our adopted value of ζ – than in the FUV-irradiated layers, due to less efficient formation and enhanced destruction by proton transfer reactions with CO, N_2, and other species. The column density of cold H_3^+ in the midplane of a protoplanetary disk remains uncertain, but its IR ro-vibrational emission is expected to be faint. In any case, JWST observations of d203-506 are not sensitive to the cold, deep midplane layers or to the inner regions of the disk near the star.

5.2. H_3^+ excitation and infrared emission in d203-506

Schroetter et al. (2025b) estimated an H_3^+ column density of $\simeq 10^{13}$ cm^{-2}, based on an local thermodynamic equilibrium (LTE) fit to their likely detection of ν_2 ro-vibrational lines in d203-506. This corresponds to an abundance $x(H_3^+)$ of a few 10^{-8}, using N_H in the disk PDR derived from JWST observations of multiple rotational lines of $H_2(v=0)$ (e.g., Berné et al. 2023, 2024). These values are broadly consistent with our PDR model results, with most of the H_3^+ column density arising from PDR zone *ii* (Figs. 1 and 6). However, it raises questions about how the ν_2 bending mode is actually excited, given the very large Einstein A_{ij} coefficients of the observed ro-vibrational lines ($\simeq 100\,s^{-1}$; e.g., Mizus et al. 2017; Bowesman et al. 2023) and the correspondingly high critical densities ($n_{cr} \approx 10^{13}$ cm^{-3}) required for collisional exitation – much higher than the typical density in the disk PDR, $n_H \approx 10^7$ cm^{-3}.

Due to the low densities (compared to n_{cr}) and the short chemical lifetime of H_3^+ in the disk PDR – on the order of a few hours and dominated by destruction reactions with electrons and H atoms – H_3^+ vibrational levels are unlikely to be thermally populated at T_{gas} through inelastic collisions. Thus, accurate modeling of the vibrational excitation requires one to incorporate the H_3^+ chemical formation and destruction rates (F and D, respectively; see Appendix E) into the statistical equilibrium equations governing the ro-vibrational level populations. In particular, when $n_H \ll n_{cr}$ and radiative pumping is not relevant (see also Zannese et al. 2025), the excess energy from an exoergic formation pathway can leave the nascent H_3^+ molecule in a vibrationally excited state, thereby driving much of the observed IR ro-vibrational emission.

To test whether the predicted physical conditions and H_3^+ chemistry in the PDR component of d203-506 can reproduce the reported H_3^+ line intensties, we used the single-slab escape-probability code GROSBETA (Black 1998; Tabone et al. 2021; Zannese et al. 2024), an enhanced version of RADEX (van der Tak et al. 2007), to compute a non-LTE excitation model of H_3^+. This code solves the statistical equilibrium equations by accounting for local chemical formation and destruction rates, ro-vibrational collisional excitation, and spontaneous

Table 2. Spectroscopic parameters of the IR H_3^+ lines reported in d203-506 and GROSBETA model predictions (see Appendix E).

Line[a] $P\|Q\|R(J'',G'')^{u,l}$	Band[a] $v_1' v_2'^{\|l'\|} \rightarrow v_1'' v_2''^{\|l''\|}$	λ (μm)	A_{ul} (s^{-1})	E_u/k_B[b] (K)	T_{ex}^{model} (K)	$F_{line}^{model,c}$ ($W\,m^{-2}$)	$F_{line}^{obs,d}$ ($W\,m^{-2}$)
$Q(5,0)$	$01^1 \rightarrow 00^0$	4.045	1.13E+02	5293.3	274.6	6.5E−22	1.7E−21
$Q(5,1)^l$	$01^1 \rightarrow 00^0$	4.045	1.09E+02	5263.8	273.4	3.1E−22	blended
$Q(5,3)^l$	$01^1 \rightarrow 00^0$	4.044	7.18E+01	5020.2	261.2	3.5E−22	blended
$Q(5,2)^l$	$01^1 \rightarrow 00^0$	4.043	9.50E+01	5174.2	269.0	2.6E−22	blended
$Q(1,0)$	$01^1 \rightarrow 00^0$	3.953	1.28E+02	3672.6	257.9	4.2E−22	2.3E−21
$R(1,0)$	$01^1 \rightarrow 00^0$	3.669	9.79E+01	3954.8	272.6	4.4E−22	2.4E−22
$R(7,6)^u$	$01^1 \rightarrow 00^0$	3.052	1.01E+02	6904.2	329.5	2.8E−22	3.8E−22
$R(7,0)$ $J',K' \rightarrow J'',K''$	$01^1 \rightarrow 00^0$	3.022	1.74E+02	8006.7	427.4	2.8E−22	7.2E−22
(5,0) → (4,3)	$00^0 \rightarrow 00^0$	16.325	3.01E−03	1736.8	750.8	1.8E−21	<6.2 E−21 (3σ)

Notes. [a]Following Lindsay & McCall (2001). [b]Determined from the lowest accessible level of H_3^+, $J,K = (1,1)$. [c]Computed using an aperture of 0.1″ (a solid angle of 2.35×10^{-13} sr), the same aperture used to extract the observational data. [d]From Schroetter et al. (2025b).

emission. We assume that the ro-vibrational level populations of the nascent H_3^+ molecule follow a Boltzmann distribution at an effective formation temperature, T_{form}. The input parameters are approximately those of disk zone *ii*: $n(H_2) = n(H) = 5\times10^6$ cm^{-3}, $T_{gas} = 1000$ K, and $N(H_3^+) = 10^{13}$ cm^{-3} (see Appendix E for more details and for the implemented inelastic collisional rates).

Based on our PDR model results, H_3^+ formation is assumed to be dominated by reaction (9) when H_2 is in its ground vibrational state ($v''=0$)[13]. Thus, we adopt $F(H_3^+) \simeq k_9(v''=0)\cdot n(H_2;v''=0)\cdot n(HOC^+) \simeq 10^{-5}$ cm^{-3} s^{-1} from the reference PDR model (see Fig. D.2), and we vary T_{form} as an input parameter. Adopting $T_{form} = 3000$ K, the resulting non-LTE excitation model (see Table 2) matches reasonably well the intensities of the unblended H_3^+ lines reported by Schroetter et al. (2025b). Furthermore, a population diagram fit to the synthetic lines from the most populous levels gives $T_{rot}(H_3^+) \simeq 1100$ K, which is on the same order as the LTE excitation temperature range estimated by Schroetter et al. (2025b). Therefore, our chemical and excitation models support the detection of H_3^+ emission in the PDR component of d203-506 and suggest that H_3^+ may be detectable in other strongly irradiated disks.

Since reaction (9) is endoergic by 1500 K when H_2 is in the ground vibrational and rotational state ($v''=0$ and $J''=0$), and $T_{form} \approx E_{H_2}(v''=0,J'')/k - 1500$ K (where $E_{H_2}(v''=0,J'')/k$ is the energy of the rotational level J'' in Kelvin), this model implies that H_3^+ formation in the disk PDR primarily proceeds via exoergic reactions of rotationally excited $H_2(v''=0, J''\geq7)$ with HOC^+. Given the relatively high densities and temperatures in the PDR component of d203-506, these rotationally excited $H_2(v''=0)$ levels are significantly populated[2]. Indeed, their associated IR emission lines are readily detected, corresponding to a rotational temperature of ~950 K (e.g., Berné et al. 2023; Zannese et al. 2024), which is very close to the predicted gas temperature in zone *ii* of the disk PDR (upper panel of Fig. 1). Consistent with this scenario, our PDR model predicts substantial populations of $H_2(v''=0, J''\geq7)$ in this zone (see the upper left panel of Fig. 6), where the abundance of H_3^+ peaks.

[13] The contribution of $H_2(v''\geq1)$ levels to H_3^+ formation via reaction (9) is less than 10% at the H_3^+ column density peak (see Fig. D.2).

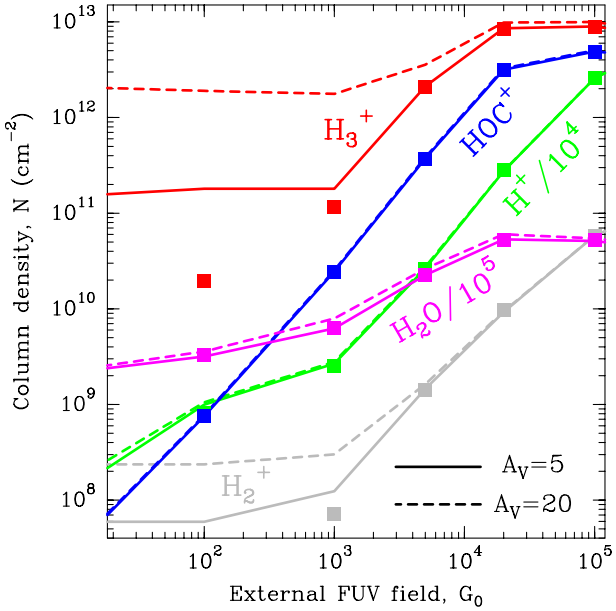

Fig. 7. Column densities of H^+, H_2^+, H_3^+, H_2O, and HOC^+ as a function of external FUV field for models with $\zeta = 10^{-16}$ s^{-1}. Continuous curves refer to column densities from $A_V = 0$ to 5 mag (tracing the disk PDR), whereas dashed curves integrate up to 20 mag (tracing colder gas). The filled squares refer to $A_V = 0$ to 5 mag models with $\zeta = 10^{-17}$ s^{-1}.

5.3. H_3^+ column density as a function of external G_0, ζ, and dust grain properties

To isolate the role of increasing G_0 and varying ζ cosmic-ray ionization rates, Fig. 7 shows the results of a grid of constant-density models ($n_H = 10^7$ cm^{-3}) for different strengths of the external FUV field and for a constant $\zeta = 10^{-16}$ s^{-1}. This plot shows increasing column densities of H^+, H_2^+, H_3^+, H_2O, and HOC^+ as a function of G_0. Among these species, $N(HOC^+)$ is a particularly good tracer of G_0. The continuous curves represent column densities integrated up to $A_V = 5$ mag (i.e., FUV-irradiated gas in the disk PDR), whereas the dashed lines show column densities integrated up to $A_V = 20$ mag (i.e., including FUV-shielded gas representative of the cold disk midplane). When the two

curves are close, it indicates that most of the column density of a given species arises from FUV-irradiated gas, near the disk surface, and not from the cold midplane. For $G_0 < 10^3$, the column densities of these species increase slowly with G_0. In this lower-irradiation regime, most of the H_3^+ and H_2^+ column density originates from colder gas, partially FUV-shielded, whereas H^+, HOC^+, and H_2O continue to primarily trace the warmer outer disk surface and wind. We recall that our models do not apply to the much denser and hot inner disk regions close to the host star ($r <$ a few astronomical units), where water vapor is highly abundant (with $N(H_2O) \gtrsim 10^{18}$ cm^{-2}; e.g., Carr & Najita 2008; Pontoppidan et al. 2010; Riviere-Marichalar et al. 2012; Du & Bergin 2014; van Dishoeck et al. 2021; Bosman et al. 2022; Banzatti et al. 2023; van Dishoeck et al. 2023; Smith et al. 2025).

The curves in Fig. 7 represent models with the same value of ζ. Nevertheless, $N(H^+)$, $N(H_2^+)$, and $N(H_3^+)$ increase significantly with G_0, particularly in the high-irradiation regime ($G_0 > 10^3$). This trend is a clear signature of FUV-driven chemistry and ionization. In the disk's PDR component, the column density of these species trace the strength of the FUV field, which triggers an active high-temperature photochemistry. To assess the role of ζ in this PDR chemistry, the filled squares in Fig. 7 represent column densities – integrated up to $A_V = 5$ mag – from models with $\zeta = 10^{-17}$ s^{-1} (a tenfold decrease in the ionization rate). In the PDR component of a strongly irradiated disk ($G_0 \gtrsim 10^3$), models with different values of ζ yield very similar results. Therefore, the dependence on ζ is very weak.

The predicted water vapor column densities in the disk PDR ($\sim 10^{14}$ to several 10^{15} cm^{-2}) are not high enough to reduce the FUV opacity through water self–shielding (Bethell & Bergin 2009; Bosman et al. 2022), and are also insufficient to produce detectable IR H_2O rovibrational emission due to very subthermal collisional excitation and ongoing photodissociation (Zannese et al. 2024). Nonetheless, any dynamical process occurring on timescales comparable to the chemistry – such as the advection of water-ice–coated grains into the PDR surface by the photoevaporative flow (e.g., Maillard et al. 2021; Coleman et al. 2025), followed by ice-mantle photo- and thermal-desorption (e.g., Walsh et al. 2013; Portilla-Revelo et al. 2025) – could enhance the abundance of water vapor at the outer disk surface, and consequently increase the abundances of HOC^+ and H_3^+ beyond our predictions. Alternatively, efficient grain growth, settling to the midplane, and radial drift may progressively remove these icy grains from the upper disk, reducing the gaseous oxygen abundance in the PDR (e.g., Öberg & Bergin 2016; Coleman et al. 2025) and, indirectly, the abundance of H_3^+.

The adopted grain-size distribution also impacts the FUV opacity, and thus the penetration of external FUV radiation. Our choice of the size distribution exponent and the a_{min} and a_{max} radii (Sect. 3) is consistent with the modest grain growth expected in the upper layers of a young irradiated disk (e.g., Störzer & Hollenbach 1999). However, over time, the smallest dust grains are expected to be entrained in the photoevaporative wind (e.g., Facchini et al. 2016). Both grain growth and dust entrainment reduce σ_{ext}^{d} (and increase the dust albedo and anisotropy of the scattered FUV radiation), thereby lowering the FUV opacity and enhancing the penetration of FUV photons (Goicoechea & Le Bourlot 2007). A lower σ_{ext}^{d} value results in a more extended C^+ layer and an increased HOC^+ column density. However, the higher electron density at the H_3^+ abundance peak enhances its destruction, thereby slightly reducing the H_3^+ column density. A model with more substantial grain growth, $\sigma_{ext}^{d} = 3.5 \times 10^{-22}$ cm^2 H^{-1} at 1000 Å, results in a factor $\sim$1.3 lower $N(H_3^+)$ than the reference model. Detections of H_3^+ in other irradiated disks will help to constrain these different scenarios.

5.4. Additional plausible pathways for H_3^+ formation

Several studies have explored alternative H_3^+ formation mechanisms in other astrophysical environments. Most of these mechanisms involve reactions with electronically excited states of atomic hydrogen and molecular hydrogen; for instance,

$$H_2^* \,(\text{Rydberg}) + H_2 \rightarrow H_3^+ + H + e^-, \tag{16}$$

which is a chemiionization process, as well as

$$H^* \,(n = 2, ...) + H_2 \rightarrow H_3^+ + e^-, \tag{17}$$

which is an associative ionization (e.g., Dehmer & Chupka 1995). In addition, associative ionization involving ground-state and excited states of atomic hydrogen may contribute. That is,

$$H\,(1s) + H(n > 2) \rightarrow H_2^+ + e^-, \tag{18}$$

which is endoergic by $\sim$12 770 K. The importance of this process was emphasized by Rawlings et al. (1993), and there is both experimental and theoretical support (Urbain et al. 1991, 1992; Hörnquist et al. 2023). The rate coefficient is small for $n = 2$ at temperatures of interest, but for $n > 2$, the process is relatively fast (the reaction becomes exoergic). Its contribution to the production of H_2^+ and H_3^+ will be limited by the populations of high-n states of atomic hydrogen. In the context of protoplanetary disks externally irradiated by both EUV and FUV radiation, recombination near the ionization front might contribute to $H(n > 2)$. However, we suspect that the resonant trapping of Lyman line photons in a very thin layer of the PDR might be a bigger effect in populating excited states. While these associative ionization processes likely produce lower H_3^+ column densities compared to the photochemistry and reactions discussed in the previous sections, they may play a larger role in environments such as centers of active or star-forming galaxies. In particular, X-ray- or cosmic-ray-dominated galaxies would naturally have a thicker zone where H, $H(n > 2)$, and H^+ coexist than star-powered (PDR) galaxies.

All in all, UV- and X-ray-driven H_3^+ formation may be relevant also in the inner disk regions (near the host star) as well as in other environments such as exoplanet atmospheres – where H_3^+ acts as an important coolant (e.g., Koskinen et al. 2007; Khodachenko et al. 2015) – and the early Universe (e.g., Lepp et al. 2002; Glover & Brand 2003; Coppola et al. 2011, 2013). Our state-dependent rate constants (Table 1) may be valuable for modeling these environments and support the prospect of new H_3^+ detections with JWST (e.g., Richey-Yowell et al. 2025).

6. Summary and conclusions

We have presented a detailed photochemical model of the PDR component of a protoplanetary disk – comprising the outer disk surface and photoevaporative wind – exposed to strong external FUV radiation. We have revisited key FUV-driven gas-phase reactions leading to H_3^+ formation, including new state-to-state dynamical calculations of the vibrational-state v-dependent rate constants for reactions of $H_2(v)$ with HOC^+ and H^+. In addition, we have modeled the photoionization of vibrationally excited $H_2(v \geq 4)$ by FUV, a process new to disk and PDR models.

These reactions dominate the formation of H_3^+ in the disk PDR, largely independent of the cosmic-ray ionization rate. We conclude that the IR line emission reported by Schroetter et al. (2025b) is consistent with the presence of H_3^+ in the PDR component of d203-506. However, our results indicate that H_3^+ is not a reliable tracer of ζ in this component, but instead primarily traces the strength of the external FUV field (G_0) and gas-phase photochemical processing. Under the conditions of this disk PDR ($G_0 \simeq 2 \times 10^4$ and $n_H = 10^7$ cm^{-3}), we predict a peak H_3^+ abundance of $\gtrsim 10^{-8}$ in the irradiated disk surface – corresponding to a column density of $N(H_3^+) \lesssim 10^{13}$ cm^{-2} – where HOC^+ is also abundant and plays a dominant role in driving the formation of H_3^+. This reactive molecular ion is ultimately linked to the enhanced abundances of C^+ (i.e., due to FUV radiation) and H_2O (see also Portilla-Revelo et al. 2025).

Given the relatively low densities (compared to the critical densities of the IR H_3^+ $\nu_2 = 1 \rightarrow 0$ lines) and the short chemical lifetime of H_3^+ in the disk PDR, H_3^+ rovibrational levels are unlikely to be thermalized by inelastic collisions with H_2, H, or e^-. A coupled non-LTE excitation and chemical formation model, with the typical physical conditions of the disk PDR ($n_H \simeq 10^7$ cm^{-3} and $T_{gas} \simeq 1000$ K), reproduces the IR H_3^+ line intensities reported by Schroetter et al. (2025b), provided that formation pumping following exoergic reactions drives most of the H_3^+ vibrational excitation. The model supports a scenario in which reactions between rotationally excited H_2 ($v'' = 0, J'' \geq 7$) and HOC^+ account for the reported H_3^+ line intensities in d203-506.

Our models show that the abundances of key molecular species (notably molecular radicals and reactive ions) are significantly enhanced in the PDR component of externally irradiated disks. However, their exact abundance depends both on the exact G_0/n_H value and on grain and PAH properties, which are not well constrained in many disks. Furthermore, the observable IR ro-vibrational spectrum ultimately depends on the underlying excitation mechanism, which is often closely tied to the species' chemical formation and destruction. Upcoming spectroscopic surveys with JWST and ALMA, targeting tens of protoplanetary disks in clustered environments (e.g., Planet formation environments collaboration 2025), will reveal this chemistry in larger disk samples. The presence of IR H_3^+ emission will be another signature of FUV-driven chemistry and photochemical processing. It remains to be seen whether face-on disks also exhibit H_3^+ features from their inner regions near the host star.

Acknowledgements. We thank the referee for the careful reading of our manuscript and the constructive report. We also thank the PDRs4All team for stimulating discussions over the past few years. JRG and OR thank the Spanish MCINN for funding support under grants PID2023-146667NB-I00 and PID2021-122549NB-C21. We thank the PCMI of CNRS/INSU with INC/INP, co-funded by CEA and CNES.

References

Adams, F. C. 2010, ARA&A, 48, 47
Aguado, A., Roncero, O., & Sanz-Sanz, C. 2021, PCCP, 23, 7735
Agúndez, M., Goicoechea, J. R., Cernicharo, J., Faure, A., & Roueff, E. 2010, ApJ, 713, 662
Andrianarijaona, V. M., Rada, J. J., Rejoub, R., & Havener, C. C. 2009, J. Phys.: Conf. Ser., 194, 012043
Andrianarijaona, V. M., Wegley, L. M., Watson, A. Z., et al. 2019, AIP Conf. Proc., 2160, 070005
Anicich, V. G., & Futrell, J. H. 1984, Int. J. Mass Spectrom. Ion Processes, 55, 189
Aru, M. L., Maucó, K., Manara, C. F., et al. 2024, A&A, 692, A137
Aslan, E., Bulut, N., Castillo, J. F., et al. 2012, J. Phys. Chem A, 116, 132
Bally, J., O'Dell, C. R., & McCaughrean, M. J. 2000, AJ, 119, 2919
Banzatti, A., Pontoppidan, K. M., Pére Chávez, J., et al. 2023, AJ, 165, 72
Bergin, E., Alexander, C., Drozdovskaya, M., Gounelle, M., & Pfalzner, S. 2024, in Comets III, eds. K. J. Meech, M. R. Combi, D. Bockelée-Morvan, S. N. Raymodn, & M. E. Zolensky, 3
Berné, O., Martin-Drumel, M.-A., Schroetter, I., et al. 2023, Nature, 621, 56
Berné, O., Habart, E., Peeters, E., et al. 2024, Science, 383, 988
Bethell, T., & Bergin, E. 2009, Science, 326, 1675
Birnstiel, T., Dullemond, C. P., Zhu, Z., et al. 2018, ApJ, 869, L45
Black, J. H. 1998, Faraday Discuss., 109, 257
Black, J. H., & Dalgarno, A. 1977, ApJS, 34, 405
Bosman, A. D., Bergin, E. A., Calahan, J., & Duval, S. E. 2022, ApJ, 930, L26
Bowesman, C. A., Mizus, I. I., Zobov, N. F., et al. 2023, MNRAS, 519, 6333
Boyden, R. D., & Eisner, J. A. 2020, ApJ, 894, 74
Boyden, R. D., & Eisner, J. A. 2023, ApJ, 947, 7
Boyden, R. D., Emig, K. L., Ballering, N. P., et al. 2025, ApJ, 983, 81
Brittain, S. D., & Rettig, T. W. 2002, Nature, 418, 57
Carr, J. S., & Najita, J. R. 2008, Science, 319, 1504
Chajia, M., & Levine, R. D. 1999, Phys. Chem. Chem. Phys., 1, 1205
Chambaud, G., Levy, B., Millie, P., et al. 1980, J. Phys. B At. Mol. Phys., 13, 4205
Champion, J., Berné, O., Vicente, S., et al. 2017, A&A, 604, A69
Chu, T.-S., & Han, K.-L. 2005, J. Phys. Chem. A, 109, 2050
Cleeves, L. I., Adams, F. C., & Bergin, E. A. 2013, ApJ, 772, 5
Cleeves, L. I., Bergin, E. A., Qi, C., Adams, F. C., & Öberg, K. I. 2015, ApJ, 799, 204
Coleman, G. A. L., Haworth, T. J., & Qiao, L. 2025, MNRAS, 539, 1190
Coppola, C. M., Longo, S., Capitelli, M., Palla, F., & Galli, D. 2011, ApJS, 193, 7
Coppola, C. M., Galli, D., Palla, F., Longo, S., & Chluba, J. 2013, MNRAS, 434, 114
Dalgarno, A. 2006, PNAS, 103, 12269
Dehmer, P. M., & Chupka, W. A. 1995, J. Phys. Chem., 99, 1686
del Mazo-Sevillano, P., Félix-González, D., Aguado, A., et al. 2024, Mol. Phys., e2183071
Desch, S., & Miret-Roig, N. 2024, Space Sci. Rev., 220, 76
Díaz-Berríos, J. K., Guzmán, V. V., Walsh, C., et al. 2024, ApJ, 969, 165
Drossart, P., Maillard, J. P., Caldwell, J., et al. 1989, Nature, 340, 539
Du, F., & Bergin, E. A. 2014, ApJ, 792, 2
Errea, L. F., Macías, A., Méndez, L., Rabadán, I., & Riera, A. 2001, Phys. Rev. A, 65, 010701
Errea, L. F., Macias, A., Méndez, L., Rabadán, I., & Riera, A. 2005, Nucl. Instrum. Methods Phys. Res. B, 235, 362
Facchini, S., Clarke, C. J., & Bisbas, T. G. 2016, MNRAS, 457, 3593
Félix-González, D., del Mazo-Sevillano, P., Aguado, A., et al. 2025, A&A, 693, A181
Ford, A. L., Docken, K. K., & Dalgarno, A. 1975, ApJ, 200, 788
Freeman, A., & Williams, D. A. 1982, Ap&SS, 83, 417
Freeman, C. G., Knight, J. S., Love, J. G., & McEwan, M. J. 1987, Int. J. Mass Spectrom. Ion Processes, 80, 255
Fuente, A., Rodrıguez-Franco, A., Garcıa-Burillo, S., Martın-Pintado, J., & Black, J. H. 2003, A&A, 406, 899
Geballe, T. R., & Oka, T. 1996, Nature, 384, 334
Geballe, T. R., Jagod, M. F., & Oka, T. 1993, ApJ, 408, L109
Geballe, T. R., Goto, M., Usuda, T., Oka, T., & McCall, B. J. 2006, ApJ, 644, 907
Ghosh, S., Sahoo, T., Adhikari, S., Sharma, R., & Varandas, A. J. C. 2015, J. Phys. Chem. A, 119, 12392
Glover, S. C. O., & Brand, P. W. J. L. 2003, MNRAS, 340, 210
Goicoechea, J. R., & Le Bourlot, J. 2007, A&A, 467, 1
Goicoechea, J. R., & Roncero, O. 2022, A&A, 664, A190
Goicoechea, J. R., Pety, J., Gerin, M., Hily-Blant, P., & Le Bourlot, J. 2009, A&A, 498, 771
Goicoechea, J. R., Pety, J., Cuadrado, S., et al. 2016, Nature, 537, 207
Goicoechea, J. R., Cuadrado, S., Pety, J., et al. 2017, A&A, 601, L9
Goicoechea, J. R., Aguado, A., Cuadrado, S., et al. 2021, A&A, 647, A10
Goicoechea, J. R., Le Bourlot, J., Black, J. H., et al. 2024, A&A, 689, L4
Goicoechea, J. R., Pety, J., Cuadrado, S., et al. 2025, A&A, 696, A100
Gómez-Carrasco, S., & Roncero, O. 2006, J. Chem. Phys., 125, 054102
Gómez-Carrasco, S., González-Sánchez, L., Aguado, A., et al. 2012, J. Chem. Phys., 137, 094303
González-Lezana, T., & Honvault, P. 2017, Monthly Not. Roy. Astron. Soc., 467, 1294
González-Lezana, T., Aguado, A., Paniagua, M., & Roncero, O. 2005, J. Chem. Phys., 123, 194309
Goto, M., Geballe, T. R., McCall, B. J., et al. 2005, ApJ, 629, 865
Goto, M., Usuda, T., Nagata, T., et al. 2008, ApJ, 688, 306
Grozdanov, T. P., & Solov'ev, E. A. 1982, J. Phys. B, 15, 1195
Habart, E., Peeters, E., Berné, O., et al. 2024, A&A, 685, A73
Habing, H. J. 1968, Bull. Astron. Inst. Netherlands, 19, 421
Haworth, T. J., & Owen, J. E. 2020, MNRAS, 492, 5030
Haworth, T. J., Reiter, M., O'Dell, C. R., et al. 2023, MNRAS, 525, 4129
Herbst, E., & Woon, D. E. 1996, AstroPhys. J., L113

Herbst, E., & Klemperer, W. 1973, ApJ, 185, 505
Hilico, L., Billy, N., Grémaud, B., & Delande, D. 2000, Eur. Phys. J. D, 12, 449
Hollenbach, D. J., & Tielens, A. G. G. M. 1999, Rev. Mod. Phys., 71, 173
Hörnquist, J., Hedvall, P., Orel, A. E., & Larson, A. 2023, Phys. Rev. A, 108, 052811
Huang, S., Portegies Zwart, S., & Wilhelm, M. J. C. 2024, A&A, 689, A338
Ichihara, A., Shirai, T., & Yokoyama, K. 1996, J. Chem. Phys., 105, 1857
Ichihara, A., Iwamoto, O., & Janev, R. K. 2000, J. Phys. B At. Mol. Phys., 33, 4747
Indriolo, N., & McCall, B. J. 2012, ApJ, 745, 91
Ishikawa, Y., Binning, R. C., & Ikegami, T. 2001, Chem. Phys. Lett., 343, 413
Jaquet, R., & Kutzelnigg, W. 2008, Chem. Phys., 346, 69
Joblin, C., Bron, E., Pinto, C., et al. 2018, A&A, 615, A129
Johnstone, D., Hollenbach, D., & Bally, J. 1998, ApJ, 499, 758
Kamisaka, H., Bian, W., Nobusada, K., & Nakamura, H. 2002, J. Chem. Phys., 116, 654
Kaplan, K. F., Dinerstein, H. L., Kim, H., & Jaffe, D. T. 2021, ApJ, 919, 27
Karpas, Z., Anicich, V., & Huntress, W. T. 1979, J. Chem. Phys., 70, 2877
Khodachenko, M. L., Shaikhislamov, I. F., Lammer, H., & Prokopov, P. A. 2015, ApJ, 813, 50
Klippenstein, S. J., Georgievskii, Y., & McCall, B. J. 2010, J. Phys. Chem. A, 114, 278
Kokoouline, V., Faure, A., Tennyson, J., & Greene, C. H. 2010, MNRAS, 405, 1195
Komasa, J., Piszczatowski, K., Łach, G., et al. 2011, J. Chem. Theory Computat., 7, 3105
Koskinen, T. T., Aylward, A. D., & Miller, S. 2007, Nature, 450, 845
Kounkel, M., Covey, K., Suárez, G., et al. 2018, AJ, 156, 84
Kraemer, W. P., & Spirko, V. 2010, Chem. Phys., 373, 170
Krstic, P. S., & Janev, R. K. 2003, Phys. Rev. A, 67, 022708
Krstić, P. S., Schultz, D. R., & Janev, R. K. 2002, Phys. Scr., 2002, 61
Kusakabe, T., Pichl, L., Buenker, R. J., Kimura, M., & Tawara, H. 2004, Phys. Rev. A, 70, 052710
Lada, C. J., & Lada, E. A. 2003, ARA&A, 41, 57
Last, I., Gilibert, M., & Baer, M. 1997, J. Chem. Phys., 107, 1451
Le, H.-A., Frankcombe, T. J., & Collins, M. A. 2010, J. Phys. Chem. A, 114, 10783
Le Bourlot, J., Roueff, E., Le Petit, F., et al. 2024, Mol. Phys., 122, e2182612
Le Petit, F., Nehmé, C., Le Bourlot, J., & Roueff, E. 2006, ApJS, 164, 506
Lepp, S., & Dalgarno, A. 1991, in Bulletin of the American Astronomical Society, 23, 1406
Lepp, S., Stancil, P. C., & Dalgarno, A. 2002, J. Phys. B At. Mol. Phys., 35, R57
Lindsay, C., & McCall, B. J. 2001, J. Mol. Spectrosc., 210, 60
Liszt, H., Lucas, R., & Black, J. H. 2004, A&A, 428, 117
Liu, J., Salumbides, E. J., Hollenstein, U., et al. 2009, J. Chem. Phys., 130, 174306
Maillard, V., Bron, E., & Le Petit, F. 2021, A&A, 656, A65
Markovic, N., & Billing, G. D. 1995, Chem. Phys., 191, 247
Markus, C. R., & McCall, B. J. 2019, J. Chem. Phys., 150, 214303
Martinez, Jr., O., Betts, N. B., Villano, S. M., et al. 2008, ApJ, 686, 1486
Mathis, J. S., Rumpl, W., & Nordsieck, K. H. 1977, ApJ, 217, 425
Maucó, K., Manara, C. F., Ansdell, M., et al. 2023, A&A, 679, A82
McCall, B. J., Hinkle, K. H., Geballe, T. R., et al. 2002, ApJ, 567, 391
McCartney, P. C. E., McGrath, C., McConkey, J. W., Shah, M. B., & Geddes, J. 1999, J. Phys. B: At. Mol. Opt. Phys., 32, 5103
Melin, H., Moore, L., Fletcher, L. N., et al. 2025, Nat. Astron., 9, 666
Miller, S., Achilleos, N., Ballester, G. E., et al. 2000, in Astronomy, Physics and Chemistry of H_3^+, 358, 2359
Miller, S., Tennyson, J., Geballe, T. R., & Stallard, T. 2020, Rev. Mod. Phys., 92, 035003
Mizus, I. I., Alijah, A., Zobov, N. F., et al. 2017, MNRAS, 468, 1717
Öberg, K. I., & Bergin, E. A. 2016, ApJ, 831, L19
Öberg, K. I., Murray-Clay, R., & Bergin, E. A. 2011, ApJ, 743, L16
O'dell, C. R., Wen, Z., & Hu, X. 1993, ApJ, 410, 696
Oka, T. 1980, Phys. Rev. Lett., 45, 531
Oka, T., & Geballe, T. R. 1990, ApJ, 351, L53
Pereira-Santaella, M., González-Alfonso, E., García-Bernete, I., et al. 2024, A&A, 689, L12
Pineau des Forets, G., Flower, D. R., Hartquist, T. W., & Dalgarno, A. 1986, MNRAS, 220, 801
Planet formation environments collaboration (Allen, M., et al.) 2025, Open J. Astrophys., 8, 54
Plasil, R., Zymak, I., Jusko, P., et al. 2012, Philos. Trans. Roy. Soc. Lond. Ser. A, 370, 5066
Pontoppidan, K. M., Salyk, C., Blake, G. A., et al. 2010, ApJ, 720, 887
Portilla-Revelo, B., Getman, K. V., Ramírez-Tannus, M. C., et al. 2025, ApJ, 985, 72
Putaud, T., Michaut, X., Le Petit, F., Roueff, E., & Lis, D. C. 2019, A&A, 632, A8
Qiao, L., Coleman, G. A. L., & Haworth, T. J. 2023, MNRAS, 522, 1939
Qu, C., & Bowman, J. M. 2016, J. Phys. Chem. A, 120, 4988
Ramírez-Tannus, M. C., Bik, A., Cuijpers, L., et al. 2023, ApJ, 958, L30
Rawlings, J. M. C., Drew, J. E., & Barlow, M. J. 1993, MNRAS, 265, 968
Richey-Yowell, T., Shkolnik, E. L., Llama, J., Sikora, J., & Smith, P. 2025, AJ, 169, 327
Riviere-Marichalar, P., Ménard, F., Thi, W. F., et al. 2012, A&A, 538, L3
Roncero, O., & del Mazo-Sevillano, P. 2025, Comput. Phys. Commun., 308, 109471
Roncero, O., Andrianarijaona, V., Aguado, A., & Sanz-Sanz, C. 2022, Mol. Phys., 120, e1948125
Ruaud, M. 2021, ApJ, 916, 103
Sahoo, T., Ghosh, S., Adhikaru, S., Sharma, R., & Varandas, A. J. C. 2014, J. Phys. Chem. A, 118, 4837
Saito, K., Hashimoto, Y., & Takayanagi, T. 2021, J. Phys. Chem. A, 125, 10750
Sanz-Sanz, C., Aguado, A., Roncero, O., & Naumkin, F. 2015, J. Chem. Phys., 143, 234303
Sanz-Sanz, C., Aguado, A., & Roncero, O. 2021, J. Chem. Phys., 154, 104104
Savage, C., & Ziurys, L. M. 2004, ApJ, 616, 966
Savin, D. W., Krstic, P. S., Haiman, Z., & Stancil, P. C. 2004, AstroPhys. J., 606, L170
Schroetter, I., Berné, O., Bron, E., et al. 2025a, Nat. Astron. [arXiv:2505.22314]
Schroetter, I., Berné, O., Goicoechea, J. R., et al. 2025b, A&A, 699, L13
Shiner, D., Gilligan, J. M., Cook, B. M., & Lichten, W. 1993, Phys. Rev. A, 47, 4042
Smith, M. A., Schlemmer, S., von Richthofen, J., & Gerlich, D. 2002, ApJ, 578, L87
Smith, S. A., Romero-Mirza, C. E., Banzatti, A., et al. 2025, ApJ, 984, L51
Spirko, J. A., Zirbel, J. J., & Hickman, A. P. 2003, J. Phys. B At. Mol. Phys., 36, 1645
Stancil, P. C., Schultz, D. R., Kimura, M., et al. 1999, A&AS, 140, 225
Stecher, T. P., & Williams, D. A. 1972, ApJ, 177, L141
Sternberg, A., & Dalgarno, A. 1995, ApJS, 99, 565
Störzer, H., & Hollenbach, D. 1999, ApJ, 515, 669
Tabone, B., van Hemert, M. C., van Dishoeck, E. F., & Black, J. H. 2021, A&A, 650, A192
Takayanagi, T., Kurosaki, Y., & Ichihara, A. 2000, J. Chem. Phys., 112, 2615
Tennyson, J., & Miller, S. 1994, Contemp. Phys., 35, 105
Tielens, A. G. G. M., & Hollenbach, D. 1985, ApJ, 291, 722
Tielens, A. G. G. M., Meixner, M. M., van der Werf, P. P., et al. 1993, Science, 262, 86
Trafton, L. M., Geballe, T. R., Miller, S., Tennyson, J., & Ballester, G. E. 1993, ApJ, 405, 761
Urbain, X., Cornet, A., Brouillard, F., & Giusti-Suzor, A. 1991, Phys. Rev. Lett., 66, 1685
Urbain, X., Cornet, A., & Jureta, J. 1992, J. Phys. B At. Mol. Phys., 25, L189
Urbain, X., de Ruette, N., Andrianarijaona, V. M., et al. 2013, Phys. Rev. Lett., 111, 203201
Ushakov, V. G., Nobusada, K., & Osherov, V. I. 2001, Phys. Chem. Chem. Phys., 3, 63
van der Tak, F. F. S., Black, J. H., Schöier, F. L., Jansen, D. J., & van Dishoeck, E. F. 2007, A&A, 468, 627
van Dishoeck, E. F., Kristensen, L. E., Mottram, J. C., et al. 2021, A&A, 648, A24
van Dishoeck, E. F., Grant, S., Tabone, B., et al. 2023, Faraday Discuss., 245, 52
van Terwisga, S. E., & Hacar, A. 2023, A&A, 673, L2
Veselinova, A., Agúndez, M., Goicoechea, J. R., et al. 2021, A&A, 648, A76
Walsh, C., Millar, T. J., & Nomura, H. 2013, ApJ, 766, L23
Watson, W. D. 1973, ApJ, 183, L17
Winter, A. J., & Haworth, T. J. 2022, Eur. Phys. J. Plus, 137, 1132
Winter, A. J., Haworth, T. J., Coleman, G. A. L., & Nayakshin, S. 2022, MNRAS, 515, 4287
Yang, T., Li, A., Chen, G. K., et al. 2021, Sci. Adv., 7, eabe4080
Yu, H.-G. 2011, Phys. Scr., 84, 028104
Zanchet, A., Agúndez, M., Herrero, V. J., Aguado, A., & Roncero, O. 2013a, AJ, 146, 125
Zanchet, A., Godard, B., Bulut, N., et al. 2013b, ApJ, 766, 80
Zanchet, A., Lique, F., Roncero, O., Goicoechea, J. R., & Bulut, N. 2019, A&A, 626, A103
Zannese, M., Tabone, B., Habart, E., et al. 2024, Nat. Astron., 8, 577
Zannese, M., Tabone, B., Habart, E., et al. 2025, A&A, 696, A99
Zhu, Y., Tian, L., Song, H., & Yang, M. 2019, J. Chem. Phys., 151, 054311
Ziurys, L. M., & Apponi, A. J. 1995, ApJ, 455, L73

Appendix A: Application to lower-density PDRs

In this Appendix we model a lower-density PDR, resembling either interstellar PDRs such as the Orion Bar or low-density photoevaporative winds. In the Orion Bar, while G_0 is also a few 10^4, the gas density is lower, about $5{\times}10^4$ cm^{-3} in the predominantly atomic PDR, and up to $\sim 10^6$ cm^{-3} in the densest molecular gas condensations (e.g., Tielens et al. 1993; Goicoechea et al. 2016). Figure A.1 shows the predicted structure of the PDR (analogous to Fig. 1) for an isobaric model (i.e., with a density gradient) with $P_{\rm th} = 10^8$ K cm^{-3} and $G_0 = 2{\times}10^4$ (e.g., Joblin et al. 2018). This lower gas density produces a more spatially extended atomic PDR, and a H/H$_2$ transition zone located about ten times deeper in A_V. In addition, the populations of the vibrationally excited H$_2(v)$ levels deviate further from thermal equilibrium populations, reaching higher abundances relative to H$_2(v = 0)$ than in the d203-506 model due to the more prominent role of FUV pumping at higher $G_0/n_{\rm H}$ values (see the upper panel of Fig. A.2). However, due to lower gas densities, lower shielding, and enhanced photodissociation, the water abundance at the PDR surface is significantly less abundant, with $x({\rm H_2O}) \lesssim 10^{-7}$.

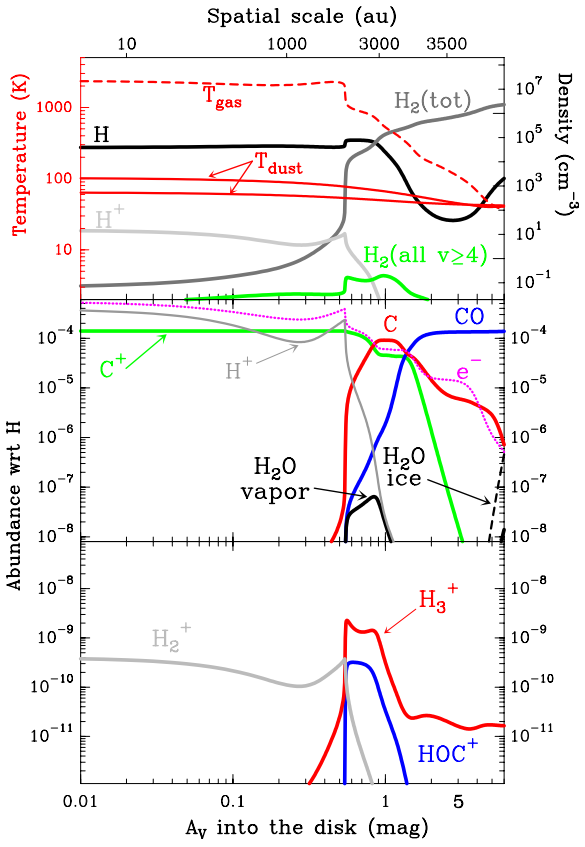

Fig. A.1. Same as Fig. 1 but for the isobaric model of the Orion Bar.

The more significant role of nonthermal H$_2(v)$ populations becomes evident when comparing the use of state-to-state versus thermal rates for reactions (2), (9) and (10). The latter approximation underestimates the H_2^+ and H_3^+ abundances by nearly two orders of magnitude in the atomic PDR zone. Compared to the d203-506 model, we find a less prominent role of the reaction H$_2(v)$ + H$^+$ in the surface layer of the PDR (partially due to lower gas temperatures), while H$_2(v \geq 4)$ photoionization becomes more significant. In addition, we predict $x(e^-) > x(C^+)$ in this zone. In any case, most of the H_3^+ column density originates from deeper layers of the molecular PDR, where the peak

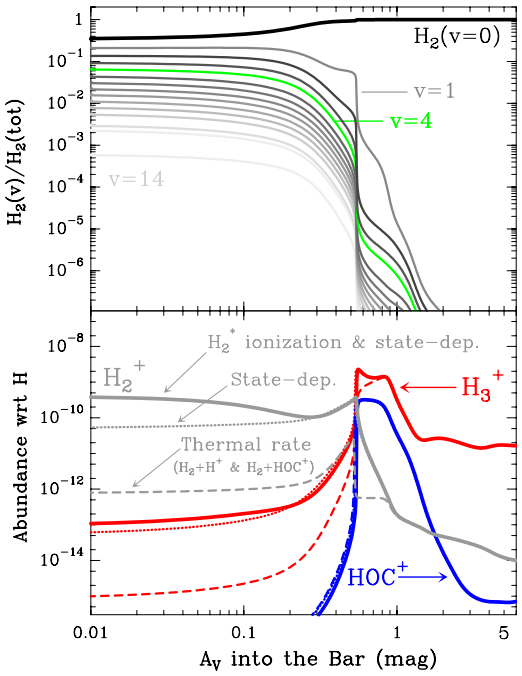

Fig. A.2. Same as Fig. 6 (left panels) but for the model of the Orion Bar.

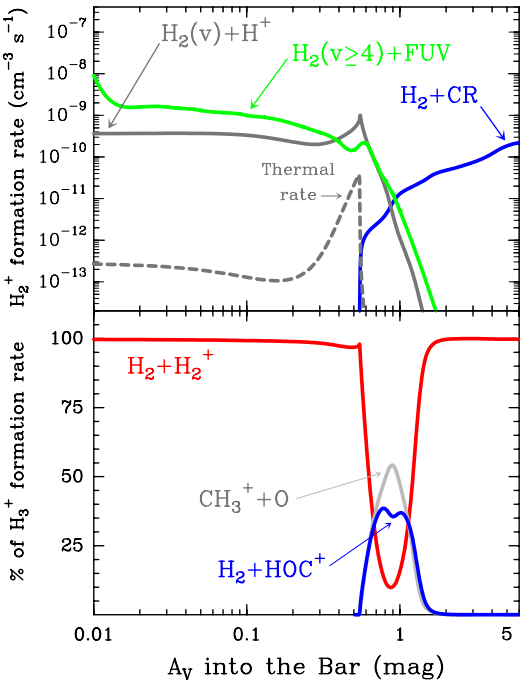

Fig. A.3. Same as Fig. 6 (right panels) but for the model of the Bar.

$x(H_3^+)$ abundance is a few $\times 10^{-9}$. This is more than an order of magnitude lower than the $x(H_3^+)$ peak in the disk model, and is a result of the two orders of magnitude lower water vapor abundance, and thus lower HOC$^+$ abundance. Instead, the reaction $CH_3^+ + O \rightarrow H_3^+ + CO$, which is also related to the presence of C$^+$, CH$^+$, and H_2^* (Berné et al. 2024; Zannese et al. 2025; Goicoechea et al. 2025), plays a more significant role (see Fig. A.3). All in all, the total H_3^+ column density in this lower-density PDR model is $\sim 10^{12}$ cm^{-3}. Still, about 70 % of the $N(H_3^+)$ column arises from FUV irradiated gas at $A_V < 1.5$ mag. In this PDR zone, H_3^+ formation is not related to ζ.

Appendix B: Charge transfer $H + H_2^+ \leftrightarrow H^+ + H_2$

The CT reactions for the formation and destruction of H_2^+ take place in three electronic states, each one corresponding to a charge in one hydrogen atom, for an electron spin zero, the singlet states. The ground adiabatic electronic state presents a deep well (see Fig. B.1), corresponding to the H_3^+ system, leading to $H^+ + H_2$ in the three possible rearrangement channels. The two adiabatic excited ones are repulsive and correlate to $H_2^+ + H$, and present high barriers for the reaction. The direct and backward reactions can result in either simple CT, with no hydrogen exchange (non-reactive), or RCT, in which both charge transfer and hydrogen exchange occur. The latter involves products forming through a rearrangement channel different from the initial one, as illustrated in Fig. B.1 by the green horizontal line, which exists only in the ground adiabatic electronic state.

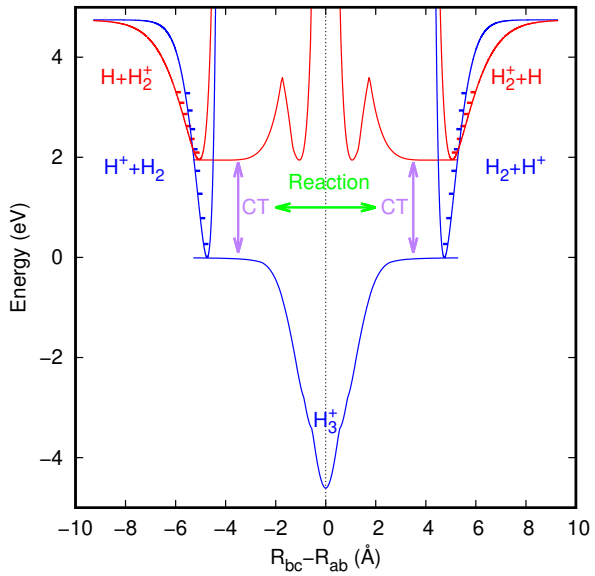

Fig. B.1. Minimum energy path of the two lower adiabatic singlet electronic states of the H_3^+ system, correlating to H_2+H^+ (ground) and H_2^+ + H (excited). Vibrational levels of diatomic fragments are indicated in blue (H_2) and red (H_2^+). The CT processes are described by electronic transitions between the two electronic state. Reaction only occurs in the ground electronic state.

Appendix B.1: Reaction $H + H_2^+(v = 0, j = 0) \rightarrow H^+ + H_2(v')$

The cross section of the reaction $H + H_2^+(v = 0, j = 0) \rightarrow H^+ + H_2$ was obtained by Sanz-Sanz et al. (2021) using a quantum wave packet method, based on the coupled electronic potential energy surfaces (PESs) calculated by Aguado et al. (2021), where a detailed description of the reaction dynamics is provided. The state-dependent CT and RCT rate constants are obtained here by numerical integration over the collision energy with a Boltzmann energy distribution, and is presented in Fig. B.2. The total (CT+RCT) rate constant is good agreement with the experimental measurement at 300 K by Karpas et al. (1979). McCartney et al. (1999) also studied this reaction, but at much higher energies of 30-100 keV, out of the scope of this study. More recently, Andrianarijaona et al. (2009, 2019) studied the H + D_2^+ isotopic variant in a broader energy range of 0.1-100 eV. Their results show a good agreement with the wave packet calculations performed using the same coupled (Roncero et al. 2022).

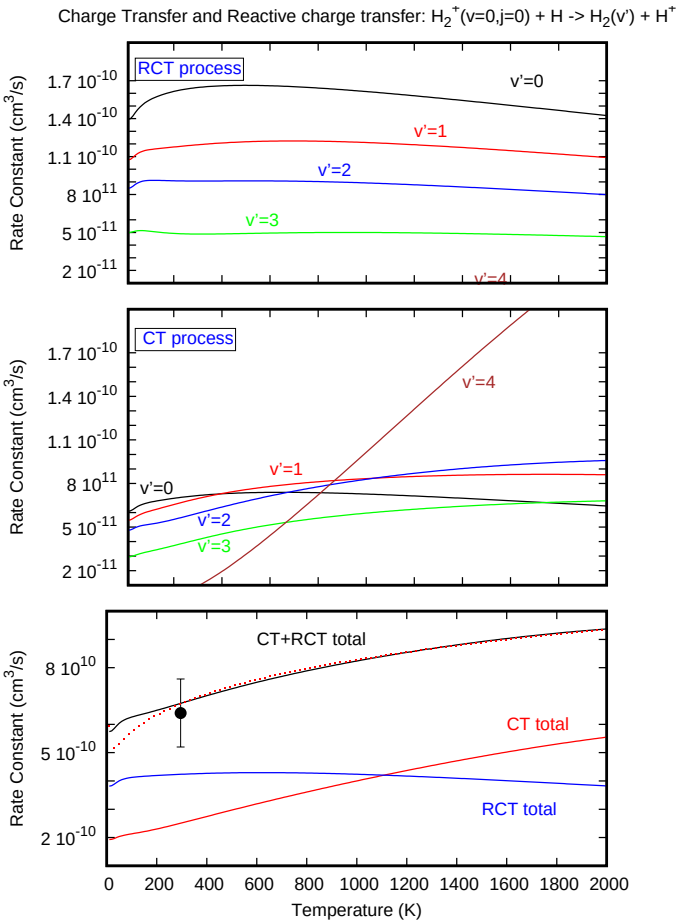

Fig. B.2. State-dependent rate constants for the reaction $H + H_2^+(v = 0, j = 0) \rightarrow H^+ + H_2$. In the bottom panel, CT, RCT and the total sum are presented. In the middle and top panels, the pure CT and RCT process are shown, respectively, showing the final state distribution of $H_2^+(v')$ vibrational states. The dotted curve represents the Arrhenius fit to the total rate constant. The point in the lower panel corresponds to the experimental measurement by Karpas et al. (1979).

Below 1000 K the RCT process dominates, involving a transition from the excited to the ground state, where the reaction takes place within the deep well due to the formation of $H_3^+(^1A')$ well. Due to the formation of long-lived $(H_3^+)^*$ complexes, the reaction behaves nearly statistically (González-Lezana et al. 2005; González-Lezana & Honvault 2017).

The vibrational distribution of $H_2(v')$ formed by the direct CT process shows some differences. $v' = 0$,1 and 2 are very close to each other, while the $v' = 4$ grows very fast once it is open at about 250 K. The reason is that the $H_2(v' = 4) + H^+$ energy is very close to that of the $H_2^+(v = 0) + H$ reactants, and this small energy difference increases the efficiency of the non-adiabatic couplings between the two electronic states from very long distances, in the so-called resonant effect (Sanz-Sanz et al. 2021).

Several approximate theoretical treatments have been applied to this reverse reaction (Last et al. 1997; Kamisaka et al. 2002; Krstić et al. 2002; Krstic & Janev 2003; Errea et al. 2005), but the present calculations and results are considered the most accurate to date, as validated by the good agreement with the experimental value reported by Karpas et al. (1979).

Appendix B.2: State-dependent rate constants for the endoergic reaction H_2 (v'') + $H^+ \rightarrow H_2^+$ (v') + H

The direct reaction H^++H_2 has been widely studied at energies above the opening of the CT H + H_2^+ channel, at 1.82 eV (Markovic & Billing 1995; Ichihara et al. 1996; Last et al. 1997; Chajia & Levine 1999; Takayanagi et al. 2000; Ushakov et al. 2001; Ichihara et al. 2000; Errea et al. 2001; Kamisaka et al. 2002; Krstic & Janev 2003; Savin et al. 2004; Kusakabe et al. 2004; Chu & Han 2005; Urbain et al. 2013; Sahoo et al. 2014; Ghosh et al. 2015). Particularly relevant for this study are the studies by Ichihara et al. (2000) and Krstić et al. (2002), in which this reaction was studied in a very large range of energies, up to a few eV, for different initial vibrational states of H_2, using approximate methods. Ichihara et al. (2000) used a quasi-classical (QCT) method including electronic transitions based in a Landau-Zener model, which is restricted to the crossing region between H_2+H^+ and H_2^+ + H (see Fig. B.1). Krstić et al. (2002) applied a quantum time independent close coupling method, but using an Infinite Order sudden (IOSA) approximation, which freezes the internal angle and decouples the helicities. Both approaches treat approximately the reactivity, making necessary a more accurate method for temperatures below –2000 K.

In this study, we use a quantum wave packet method that includes all degrees of freedom and can be considered "exact" for treating reactivity up to –2000 K. The calculations are similar to those performed for the reverse reaction (Sanz-Sanz et al. 2021), as described in Appendix B, and are carried out using the MADWAVE3 code (Roncero & del Mazo-Sevillano 2025). This code represents the Hamiltonian in reactant Jacobi coordinates within a body-fixed frame, employing grids for the internal coordinates (the Jacobi distances r and R, associated with the H_2 internuclear vector and the vector joining the H_2 center of mass with H^+, respectively), and a basis for the electronic coordinates and total angular momentum **J**, characterized by the quantum number J and its projections M and Ω on the space-fixed and body-fixed z-axes, respectively.

Due to the presence of the deep H_3^+ potential well, a large number of Ω projections is required to achieve convergence. In this work, we use $\Omega_{max} = \min(J, 15)$. The flux into individual final states of the $H_2^+(v', j')$ products is evaluated using a reactant-to-product coordinate transformation method (Gómez-Carrasco & Roncero 2006), applied separately for each J. To reduce computational cost, we explicitly calculate J = 0, 5, 10, 20, 30, 40, and 60. For intermediate J values, the state-to-state reaction probabilities are interpolated using the J-shifting method (Aslan et al. 2012).

The total CT cross section (CT + RCT) for different initial $H_2(v, j = 0)$ are shown in the bottom panel of Fig. B.3. The threshold for the CT is at 1.79 eV, so that the reaction is endothermic for $v < 4$, leading to negligible reactive cross sections below 0.4 eV for v=0-3 (see Fig. B.1). However, for $v \geq 4$ the CT reaction becomes energetically accessible and the cross section becomes important, between 50 and 200 Å^2 for v=4, 5 and 6. Qualitatively this result is similar to those reported previously by Ichihara et al. (2000) in their Fig. 1 and by Krstić et al. (2002) in Fig. 1. However, we consider the magnitude of the exact quantum results obtained in this work is considerably more precise. For example, for $v = 6$ below 2.5 eV, the total cross section is always lower than 40 Å^2 (Ichihara et al. 2000), while here is between 100-200 Å^2. The large differences is attributed to classical character of the CT, made with a simple Landau-Zenner model. The IOSA results of Krstić et al. (2002) for v=4 shows a threshold, which is absent here.

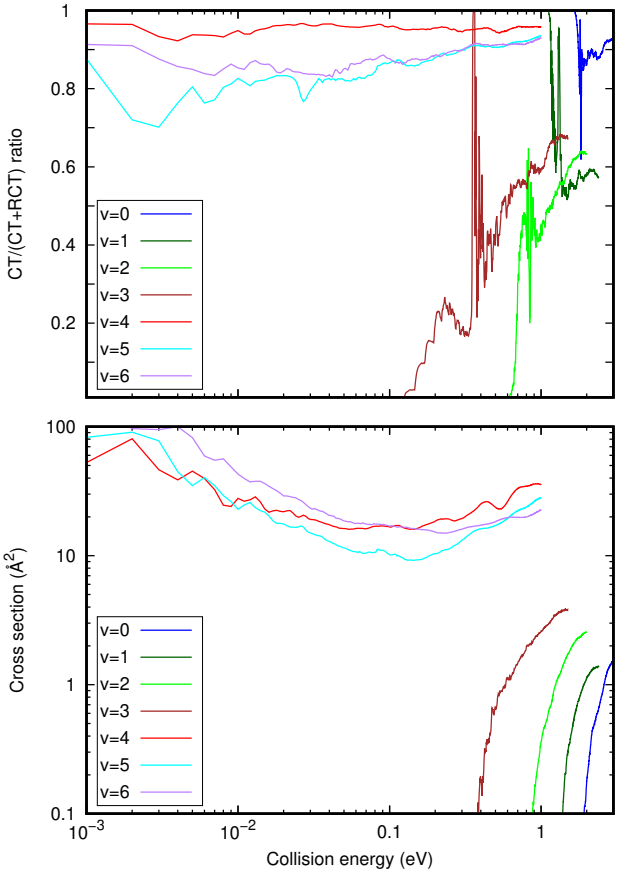

Fig. B.3. *Upper panel*: Fraction of the CT cross section as a function of v. *Botom panel*: Total reactive cross sections (CT and RCT) for the reaction H^++$H_2(v) \rightarrow H + H_2^+$ for several initial vibrational states v.

The CT/(CT+RCT) ratio shown in the top panel of Fig. B.3 demonstrates that the dominant process is the simple CT without reaction. The RCT process acounts for a maximum of 30% for $v \geq 4$, while is dominant for the lower $v < 4$. This trend is also similar to the values reported by Ichihara et al. (2000) in the low energy region. We find that for $v > 6$ the total CT cross section progressively diminish with increasing v. Moreover, it is difficult to extend the present quantum calculations calculations above $v = 6$, because it is very close to the three-body fragmentation channel, and we shall adopt here the behavior by Ichihara et al. (2000).

The CT rate constant are obtained by numerical integration of the cross section with a Boltzmann distribution. Figure 4 shows the enhancement of the reaction rate as the vibrational excitation of the initial H_2 increases, becoming very similar for $v = 4, 5$ and 6, close to the Langevin value, with a rate constant of $\simeq$ (2-4)$\times 10^{-10}$ cm^3 s^{-1}.

The final $H_2^+(v')$ products populate progressively more excited vibrational states with increasing initial $H_2(v)$, as shown in Fig. B.4. For example, for an initial state of $v = 6$, the dominant final state is $v' = 3$. Moreover, the reaction $H_2 + H_2^+(v) \rightarrow H_3^+ + H$ was recently studied for initial vibrational states v = 0–6, and it was found that, up to collision energies of 1 eV, the reactive cross section is nearly independent of v, with values very close to the Langevin limit (del Mazo-Sevillano et al. 2024). At higher collision energies, however, the reactive cross section increases with v.

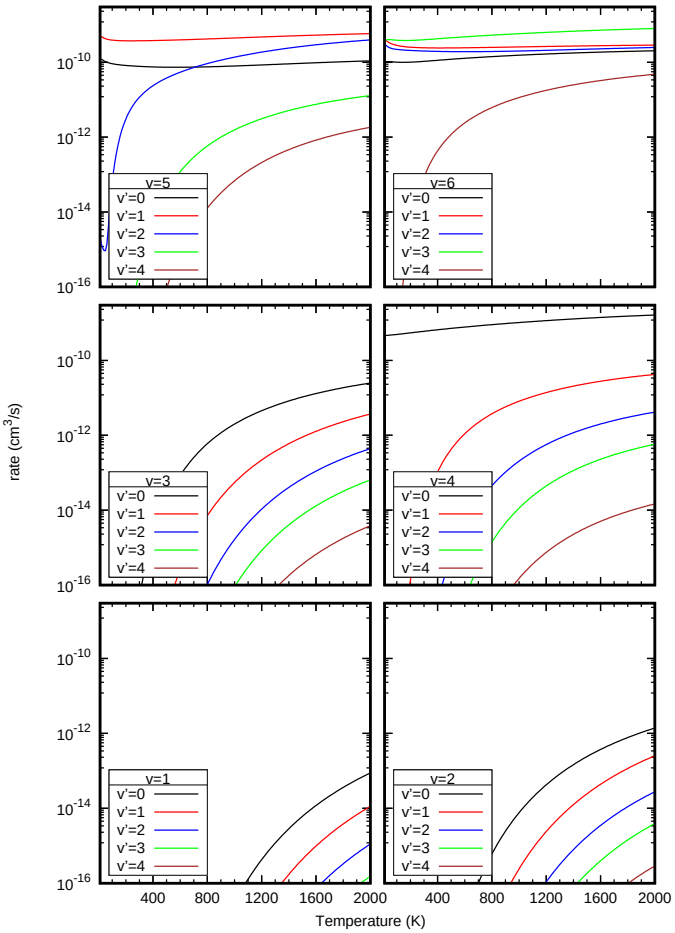

Fig. B.4. State-to-state reactive rate constants (CT and RCT) for the reaction $H^+ + H_2(v) \rightarrow H + H_2^+(v')$ considering several initial v and final v' vibrational states.

Appendix C: Photoionization of H_2^* ($v'' \geq 4$)

Figure C.1 shows the state-to-state $H_2^*(v''>4)$ photoionization cross sections adopted in our photochemical models for reaction (5). These cross sections were computed by Ford et al. (1975) and are provided for photoionization, where the product H_2^+ is formed in a specific vibrational level v'. Hence, the result is a superposition of step functions, each corresponding to a different value of v'. These calculations only consider rotational transitions $J''=1 \rightarrow J'=1$. Here we explicitly calculated the FUV photon energy thresholds (E_t) for each state-to-state process, from $v''=4$ to 14 and leading to vibrationally excited $H_2^+(v')$. Specifically, we used the energy of the $H_2(v''\geq4, J''=1)$ levels (Komasa et al. 2011) and of $H_2^+(v', J''=1)$ levels (Jaquet & Kutzelnigg 2008; Hilico et al. 2000) and computed:

$$E_t = E_I(H_2) - \Delta E(v'' - v'), \quad \text{(C.1)}$$

where E_I is the H_2 ionization energy (15.426 eV, e.g., Shiner et al. 1993) and $\Delta E(v''-v') = E_{H_2}(v'', J''=1) - E_{H_2^+}(v', J'=1)$.

Since we do not explicitly follow the vibrational excitation of H_2^+ molecules, we use $\sigma_\lambda(v'') = \sum_{v'} \sigma_\lambda(v'' \rightarrow v')$ and integrate these $\sigma_\lambda(v'')$ sections cross sections over the local FUV energy density at different disk positions (equation 6). Figure C.2 shows the resulting rates for the specific model of d203-506 (normalized to $G_0=1$). To simplify their use in the Meudon PDR code, we carried out v''-state-dependent power-law fits, of the form $\kappa_{phi}(v''; A_V) = G_0\, \kappa_0(v'')\exp(-\gamma(v'')\, A_V)$, to these rates (in s^{-1}). The $\kappa_0(v'')$ and $\gamma(v'')$ parameters are tabulated inside the code, and used to determine the total H_2^+ formation rate due to $H_2^*(v'')$, summed over all v'' levels, FUV photoionization.

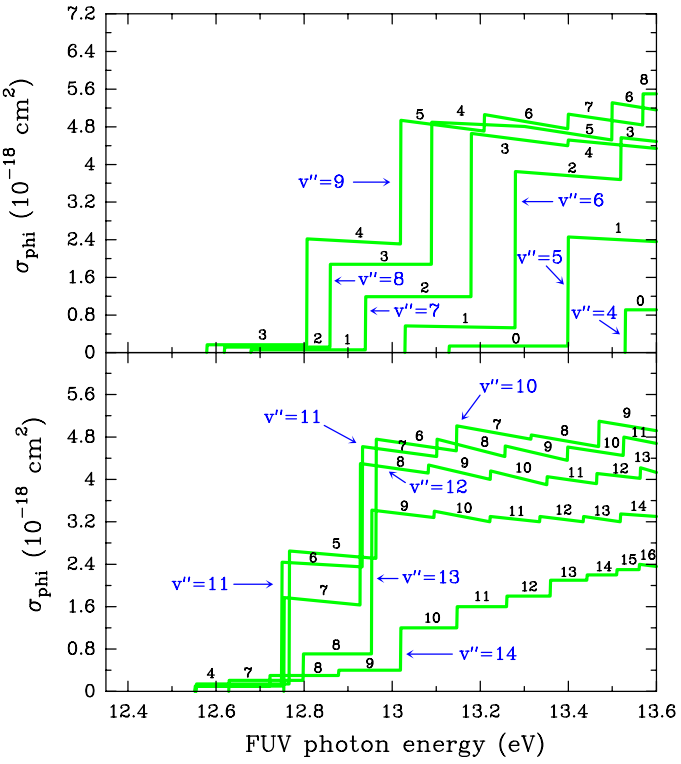

Fig. C.1. Cross sections for FUV photoionization of H_2^*, from vibrationally excited levels v'' to H_2^+ vibrationally excited levels, v', as a function of FUV photon energy (from Ford et al. 1975). Upper panel: $H_2^*(v''=4$ to 9). Lower panel: $H_2(v''=10$ to 14). The numbers (in black) on the horizontal sections of the curves denote the v' levels of H_2^+.

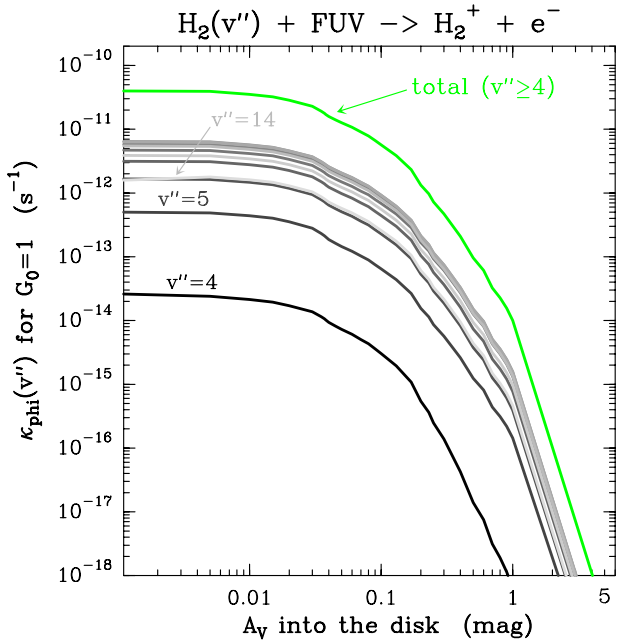

Fig. C.2. Resulting $H_2(v''\geq4)$ photoionization rates (normalized to $G_0=1$) as a function of depth into the disk after direct integration of equation (6) using the λ-dependent FUV field of our model of d203-506. In this model, the largest contribution to $H_2(v''\geq4)$ photoionization comes from the $v''=10$ level.

Appendix D: State-dependent rate constants for reaction H_2 + $HOC^+ \rightarrow H_3^+$ + CO and isomerization

The title reaction has been studied experimentally. Freeman et al. (1987) measured a rate constant of 4.7×10^{-10} cm^3 s^{-1} at 300 K. At a lower temperature of 25 K, however, Smith et al. (2002) did not detect H_3^+ formation, observing only the isomerization product HCO^+. Herbst & Woon (1996) calculated the stationary points on the corresponding potential energy surface, finding a submerged barrier. From this, they proposed that the reaction may proceed via an isomerization route forming $HCO^+ + H_2$ (a highly exothermic pathway), or alternatively form $H_3^+ + CO$, which is endothermic by 0.14 eV (including ZPEs). As a result, the latter pathway was considered unimportant.

Most theoretical studies have focused on the HOC^+/HCO^+ isomerization ratio in the H_3^+ + CO reaction (Le et al. 2010; Yu 2011; Zhu et al. 2019; Saito et al. 2021). Yu (2011) investigated the H_2 + HOC^+ reaction using on-the-fly classical trajectory simulations at a relatively low level of theory (SAC-MP2), and did not report the formation of H_3^+ products.

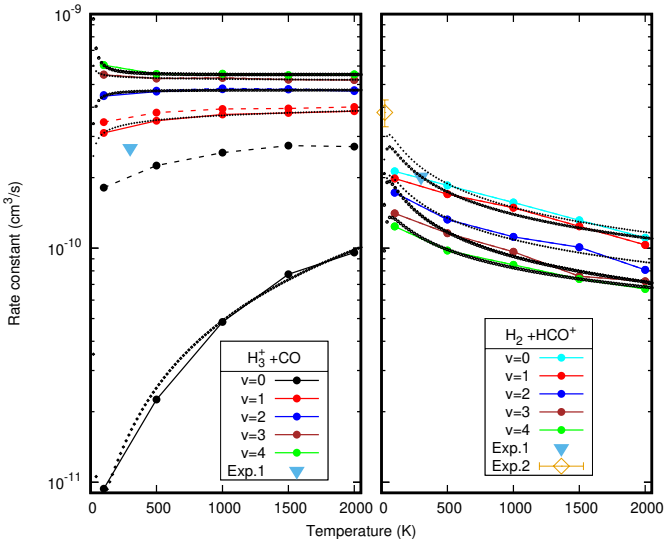

Fig. D.1. $H_2(v = 0–4,\ j = 0)$ + HOC^+, obtained using a QCT method, are shown with and without the ZPE correction for the H_3^+ ZPE. Solid lines represent the corrected results; dashed lines show the uncorrected ones. Dotted curves represent the Arrhenius fit to the ZPE-corrected rates. The yellow point in the right panel indicates the experimental rate constant reported by Smith et al. (2002), while the blue triangles represent the rate constants reported by Freeman et al. (1987).

In this work, we study the title reaction using the high-level potential energy surface (PES) developed by Zhu et al. (2019). This PES reveals an endothermic direct pathway from reactants to products, with an energy difference of 0.125 eV—slightly lower than the value reported by Herbst & Woon (1996). Along the entrance channel, the reaction dynamics can also proceed through a submerged barrier (−0.085 eV including ZPE) toward a deep H_2–HCO^+ well, from which the system evolves to $H_2 + HCO^+$ products. These products lie approximately 1.75 eV below the $H_2 + HOC^+$ reactants.

In order to study the $H_2(v$=0–4, j=0) + $HOC^+ \rightarrow H_3^+ + CO$ reaction, it is important to account for the ZPEs of both reactants and products. Here, we employ a quasi-classical trajectory (QCT) method, as implemented in the MDwQT code (Sanz-Sanz et al. 2015), in which the initial vibrational conditions of the reactants are generated using the adiabatic switching method (Grozdanov & Solov'ev 1982; Qu & Bowman 2016). This approach allows us to include the vibrational energy of H_2 in different vibrational levels, as well as that of HOC^+ in its ground vibrational state (with a ZPE of 0.336 eV, consistent with the values reported by Kraemer & Spirko (2010)).

The rate constants obtained in the $T \simeq 100$—-2000 K range are shown in Fig. D.1 for several initial vibrational states of H_2. For each case, two sets of results are presented: one including all reactive trajectories (dashed lines), and another excluding those trajectories that result in product vibrational energies below the corresponding ZPE. The H_3^+ formation is strongly affected by this correction. The ZPE-corrected results are reliable because the formation of H_3^+ proceeds through a direct mechanism. Thus, selecting trajectories with physically meaningful vibrational energies at both the beginning and the end effectively mitigates potential inaccuracies introduced by classical mechanics calculations.

For $H_2(v = 0)$, the ZPE-corrected rate constants decrease significantly with decreasing temperature. This trend is consistent with the absence of H_3^+ products in the experimental study by Smith et al. (2002). On the other hand, the rate constant measured for isomerization toward HCO^+ (yellow point in the right panel of Fig. D.1) is in good agreement with the calculated rates.

The value reported by Freeman et al. (1987) at 300 K for H_3^+ formation is much higher than our rate constant for initial $H_2(v = 0)$ but slightly lower than the calculated rates for $H_2(v = 1)$. To reconcile these differences, we suspect that the HOC^+ reactants in the Freeman et al. (1987) experiment may have been vibrationally excited. This assumption allows us to provide a coherent interpretation that integrates all available experimental and theoretical data.

Figure D.2 shows the evolution of the vibrational-state dependent H_3^+ formation rate, F (in cm^{-3} s^{-1}), for the reaction $H_2(v) + HCO^+ \rightarrow H_3^+ + CO$, after incorporating the rate constants from Fig. D.1 into our reference PDR model.

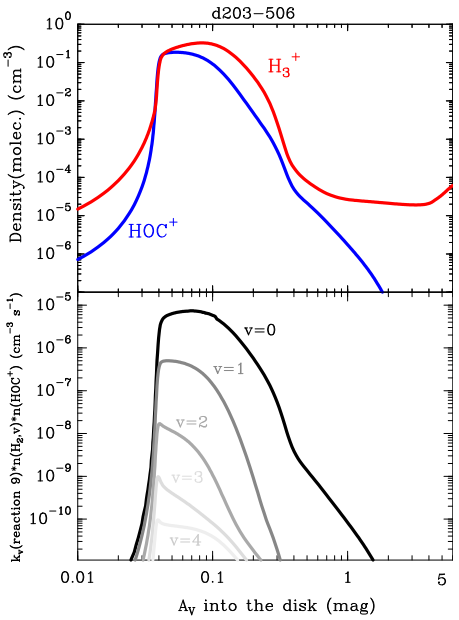

Fig. D.2. *Upper panel*: H_3^+ and HOC^+ volume densities predicted by the reference model of d203-506. *Lower panel*: Vibrational-state dependence of the H_3^+ formation rate, F in cm^{-3} s^{-1}, for reaction $H_2(v)$ +$HOC^+ \rightarrow H_3^+ + CO$, as a function of depth into the PDR.

Appendix E: Coupled non-LTE excitation and chemical formation model of H_3^+

We briefly describe the non-LTE excitation models carried out with the zero-dimensional (0D) escape-probability radiative transfer model GROSBETA (Black 1998; Tabone et al. 2021; Zannese et al. 2024), an enhanced version of RADEX (van der Tak et al. 2007). We used this model to test whether the physical conditions and H_3^+ chemistry predicted by our PDR model can reproduce the IR H_3^+ line intensities reported in d203-506 (Schroetter et al. 2025b). GROSBETA solves the statistical equilibrium equations by accounting for local chemical formation and destruction rates, ro-vibrational collisional excitation, spontaneous emission, and line opacities providing physically consistent predictions of the emergent line intensities under non-LTE excitation conditions.

A proper treatment of H_3^+ vibrational excitation must account for the chemical formation and destruction rates within the statistical equilibrium equations that govern the ro-vibrational level populations. These equations take the form:

$$\sum_{j>i} n_j A_{ji} + \sum_{j\neq i} n_j \left(B_{ji}\,\bar{J}_\nu + C_{ji}\right) + F_i = \tag{E.1}$$

$$= n_i \left(\sum_{j<i} A_{ij} + \sum_{j\neq i} \left(B_{ij}\,\bar{J}_\nu + C_{ij}\right) + D_i\right), \tag{E.2}$$

where n_i [cm^{-3}] is the population of ro-vibrational level i; A_{ij} and B_{ij} are the Einstein coefficients for spontaneous and stimulated emission, respectively; and C_{ij} [s^{-1}] is the rate of inelastic collisions. The latter is given by $C_{ij} = \sum_k \gamma_{ij,k}(T)\, n_k$, where $\gamma_{ij,k}(T)$ [cm^3 s^{-1}] are the temperature-dependent collisional rate coefficients, and k denotes collision partners H_2, H, or e^-. The term $\bar{J}_\nu$ represents the mean intensity of the radiation field averaged over the line profile and solid angle. In the above expression, F_i is the formation rate into level i per unit volume, and $n_i\, D_i$ is the destruction rate from level i per unit volume, both in cm^{-3} s^{-1}. Assuming a level-independent destruction rate ($D_i = D$), one can model the ro-vibrational level distribution of newly formed H_3^+ molecules as a Boltzmann distribution characterized by a formation temperature $T_{\rm form}$, where

$$F_i = F\, g_i\, \frac{e^{-E_i/kT_{\rm form}}}{Q(T_{\rm form})}, \tag{E.3}$$

and F [cm^{-3} s^{-1}] is the total (state-averaged) formation rate per unit volume, g_i is the degeneracy of level i, and $Q(T_{\rm form})$ is the H_3^+ partition function at the formation temperature $T_{\rm form}$.

As these are constant column density $N(H_3^+)$ excitation models, we used a normalized formation rate $F = \sum F_i$ that adopts steady-state H_3^+ abundances. That is, $F = \sum F_i = x(H_3^+)\, n_{\rm H}\, D$ [cm^{-3}s^{-1}], where x refers to the H_3^+ abundance with respect to H nuclei, and D is the chemical destruction rate in s^{-1}.

Appendix E.1: Model input

We included 748 H_3^+ vibrational-rotational levels with $J < 9$, except for the (9,9) metastable level, and nearly 29 000 radiative transitions. The spectroscopic data have been taken from the ExoMol MiZATeP data set (Mizus et al. 2017; Bowesman et al. 2023). The $H_2 + H_3^+$ and $H + H_3^+$ inelastic rotational collision rates are taken from Gómez-Carrasco et al. (2012) and Félix-González et al. (2025), respectively. The inelastic electron collision rates are taken from Kokoouline et al. (2010) plus our own Coulomb-Born rate approximation for the vibrational transitions. In addition, we have included some approximate rate coefficients for H–H_3^+ and H_2–H_3^+ vibrational collisional excitation. The typical magnitude of the relevant de-excitation rate coefficients is $\gamma_{ij} \gtrsim 10^{-11}$ cm^3 s^{-1}.

The input parameters are representative of zone *ii* in the disk PDR: $n(H_2) = n(H) = 5{\times}10^6$ cm^{-3}, $n(e) = 300$ cm^{-3}, $T_{\rm gas} = 1000$ K, and $N(H_3^+) = 10^{13}$ cm^{-2}. Based on our PDR model results, H_3^+ formation is assumed to be dominated by reaction (9) when H_2 is in its ground vibrational state ($v'' = 0$). Therefore, we adopt a formation rate of $F(H_3^+) \simeq k_9(v''{=}0) \cdot n(H_2; v''{=}0) \cdot n(HOC^+) \simeq 10^{-5}$ cm^{-3} s^{-1} (see detailed predictions in Fig D.2). Thus, the chemical destruction rate of H_3^+ is $D = F\,/\,x(H_3^+) \cdot n_{\rm H} \simeq 10^{-4}$ s^{-1} (or a lifetime of 2.8 h), adopting $x(H_3^+) = 10^{-8}$ and $n_{\rm H} = 10^7$ cm^{-3}.

Finally, we adopted an intrinsic line widths of 2.7 km s^{-1} as indicated by velocity-resolved ALMA observations of d203-506 (Berné et al. 2024; Goicoechea et al. 2024), and obtained the synthetic line flux by adopting a source emitting area with a solid angle equivalent to an aperture of 0.1″, consistent with the line fluxes extracted by Schroetter et al. (2025b) from JWST/NIRSpec observations.

Appendix E.2: Model results

Adopting a formation temperature of $T_{\rm form} = 3000\,{\rm K} \approx E_{H_2}(v'', J'')/k - 1500$ K–corresponding to H_3^+ being primarily formed via reactions between $H_2(v''{=}0; J''{\geq}7)$ and HOC^+–results in a non-LTE excitation model that is consistent the intensities of the unblended H_3^+ ro-vibrational lines reported by Schroetter et al. (2025b) to within a factor of about two. Table 2 shows the output of this excitation model.

In addition, we also find implications for the H_3^+ forbidden pure rotational emission spectrum, which has yet to be observed in the ISM. Due to its symmetric, equilateral triangular structure, H_3^+ lacks a permanent electric dipole moment. Ordinarily, this would imply that pure rotational transitions are strictly forbidden. However, the symmetry of H_3^+ is slightly broken by rotation-vibration coupling, which induces a weak dipole moment. As a result, radiative transitions between rotational levels that comply with selection rules are permitted, though they are very slow. Our model suggests that the most intense transition of H_3^+ in the parameter space of interest is the pure rotational transition $(J, K) = (5, 0) - (4, 3)$ at 16.325 μm. The transition frequency has been accurately predicted from measured combination differences by Markus & McCall (2019). Our non-LTE model predicts an intensity that is rather close to the 3σ detection limit on integrated intensity in the JWST-MIRI spectrum of d203-506. In other words, the column density of H_3^+ at $T_{\rm gas} \simeq 1000$ K cannot be much larger than 10^{13} cm^{-2}, otherwise this 16.325 μm line should be detected above the strong continuum.